Article

Different gametogenesis states uniquely impact longevity in *Caenorhabditis elegans*

Amaresh Chaturbedi ◍ & Siu Sylvia Lee ◍ ✉

Reproduction affects lifespan and fat metabolism across species, suggesting a shared regulatory axis. In *Caenorhabditis elegans*, ablation of germline stem cells leads to extended lifespan and increased fat storage. While many studies focus on germline-less *glp-1(e2144)* mutants, the hermaphroditic germline of *C. elegans* provides an excellent opportunity to study how distinct germline anomalies affect lifespan and fat metabolism. We compare metabolomic, transcriptomic, and genetic pathway differences among three sterile mutants: germline-less *glp-1*, feminized *fem-3*, and masculinized *mog-3*. All three accumulate excess fat and share expression changes in stress response and metabolism genes. However, *glp-1* mutants exhibit the most robust lifespan extension, *fem-3* mutants live longer only at certain temperatures, and *mog-3* mutants are markedly short-lived. The extended lifespan in *fem-3* mutants require *daf-16/FOXO*, as in *glp-1* mutants. In contrast, *daf-16* is dispensable for the already shortened lifespan of *mog-3* mutants. Interestingly, *mog-3* partially mimics male/mating-induced demise, offering a simplified model to study metabolic and reproductive trade-offs underlying this phenomenon. Our data indicate that disrupting specific germ cell populations leads to distinct and complex physiological and longevity outcomes. These findings highlight the importance of investigating sex-dependent differences and underlying mechanisms to fully understand and potentially modulate these relationships.

Reproduction is an energy-intensive process and can divert resources from somatic maintenance[1], and diminished reproduction often correlates with increased lifespan in diverse organisms, including mammals[2–11]. The simple nematode *C. elegans* largely present as self-fertile hermaphrodites but can also be mated by males, making it a versatile model to investigate the complex relationship between reproduction, resource allocation, and longevity. Over the past three decades, studies in *C. elegans* have demonstrated that the removal of germline stem cells—either through laser ablation or genetic mutations, such as the temperature-sensitive *glp-1(e2144)* mutant—leads to lifespan extension and significant alterations in fat metabolism in hermaphrodites[2,6,12]. Notably, lifespan extension was found to be proportional to the inhibition of germline proliferation, indicating a direct influence of germline activity on longevity[2]. Subsequent studies revealed that germline-mediated alteration of longevity and fat metabolism are primarily regulated through signaling communication with the intestine, involving several key factors that function via or within the intestine[12–17]. Despite significant advances, the precise mechanisms by which various germ cell populations influence intestinal physiology and contribute to longevity remain only partially understood.

Normal germline development in *C. elegans* hermaphrodites involves mitotic proliferation of the germline stem cells, regulated by Notch signaling, including the GLP-1 Notch receptor, followed by a transition to meiosis[18]. The sex determination pathway helps to regulate differentiation of the meiotic germ cells first into sperm during L4 stage, which then switch to differentiation into oocytes[18]. Defects in components of the sex determination pathway result in mutants that fail to differentiate into mature gametes appropriately[18,19]. Feminization (*fem*) mutants, which do not produce sperm but produce oocytes,

Department of Molecular Biology and Genetics, Cornell University, Ithaca, NY, USA. ✉e-mail: sylvia.lee@cornell.edu

and can reproduce after mating and effectively functioning as females[20]. In contrast, masculinization (*mog*) mutants produce only sperm, but lack male copulatory architecture, thus making them infertile; these mutants may be thought of as "male" in terms of germ cells but possess hermaphroditic somatic features[20]. Therefore, the hermaphroditic nature of *C. elegans* germline presents a unique opportunity to explore the effects of different gametogenesis processes on metabolism, physiology, and aging, and offers a promising avenue for deeper investigation of these mechanisms.

To fill the existing knowledge gaps, we focused on three sterile mutants, including the well-studied *glp-1*, which is germline-deficient, as well as *fem-3* and *mog-3* that represent feminized and masculinized mutants, respectively. Comparative analysis revealed that although they all show increased fat storage, their lifespans vary. Specifically, germline-less and feminized mutants live longer, the latter at certain temperatures, while masculinized mutants have shorter lifespans, indicating that fat accumulation alone does not ensure a longer life in reproductive deficient mutants. To deepen our understanding of this connection at a molecular level, we examined lipid composition, transcriptomic profiles, and interactions with crucial genetic elements in three mutants representing distinct forms of self-sterility. We found that the long-lived *glp-1(-)* and *fem-3(-)* mutants employ a similar life-span extension mechanism converging on the transcription factor DAF-16/FOXO, which is partially stimulated by excess lipid. In contrast, the short-lived *mog-3(-)* mutant appears to recapitulate molecular changes similar to those of male/mating-induced demise (MID)[21]. Therefore, *mog* mutants likely provide a simplified model to further understand the molecular mechanisms of MID, bypassing the complexities and variability associated with actual mating. Overall, our study highlights the intricate relationships between germ cell development, fat metabolism, and lifespan, offering valuable insights that are likely relevant to diverse species, including mammals.

Results

Different types of self-sterile mutants accumulated excessive lipids but displayed varied lifespans

To explore the effects of germline development and reproduction on fat accumulation and lifespan in *C. elegans*, we investigated 10 candidate genes that, when inactivated, resulted in different types of self-sterility (Fig. 1a, Source Data). Based on currently available annotations, we tested: *glp-1* and *iff-1*, which regulate germline proliferation[22,23]; *gld-1* and *pro-1*, which regulate meiosis[24,25]; *mog-3*, which regulates oogenesis[26]; *fbf-1/2*, which regulate the switch from mitosis to meiosis[27]; *fem-1*, *fem-3*, and *fog-3*, which regulate spermatogenesis[20]. Irrespective of the mode of sterility, RNAi against each of the genes tested induced worms to accumulate higher levels of lipids based on oil red O (ORO) staining (Supplementary Fig. 1a, Source Data). The accumulated lipids in the germline-less *glp-1* mutant have been shown to be key to its extended longevity[14]. Interestingly, despite the accumulated levels of lipids, at 20 °C, only RNAi knockdown of *glp-1* and *iff-1* led to an increase in lifespan, whereas knockdown of *mog-3, fbf-1/2, mpk-1, gld-1*, and *pro-1* resulted in shortened lifespan, and inactivation of *fem-1, fem-3* and *fog-3* showed no change in lifespan compared to wild-type N2 (WT) (Supplementary Fig. 1b; Source Data). We further validated the RNAi findings using the available loss-of-function mutants and found similar lifespan phenotypes (Supplementary Fig. 1c; Source Data).

To further understand the connection between reproduction, longevity, and lipid metabolism, we selected three mutants, representing three different types of self-sterility, for detailed studies: the germline-less *glp-1(e2144)*, the feminized *fem-3(e1996)* and the masculinized *mog-3(q74)*. Since *glp-1(e2144)* is a temperature-sensitive mutant, we examined how different temperatures can affect the lifespans of these strains. We observed that *glp-1(-)* mutants and *fem-3(-)* mutants showed longer lifespans than WT, and *mog-3(-)* mutants lived

shorter, when grown at 25 °C then shifted to 20 °C, or when grown at 25 °C without the temperature shift (Fig. 1b, c; Source Data). At 15 °C, we observed similar results where *glp-1(-)* and *fem-3(-)* mutants lived longer and *mog-3(-)* mutants lived shorter than WT, although all strains had a longer lifespan at 15 °C compared to 25 °C, as expected (Supplementary Fig. 1d, Source Data). Taken together, at all temperatures tested (15, 20, and 25 °C), *mog-3(-)* mutants lived shorter, and *glp-1(-)* mutants lived longer than WT. The *fem-3(-)* mutant also exhibited a longer lifespan at 25 °C and 15 °C; however, at 20 °C, we observed no difference in lifespan between *fem-3(-)* mutant and WT. Based on these results, we chose to conduct our follow-up analyses using worms grown at 25 °C.

We next quantified the lipid levels in the three mutants using several different methods. Studies have shown that fatty acids and derivatives thereof, such as oleic acid, oleoylethanolamide, and α-linolenic acid, are already altered in germlineless mutants relative to WT by day 1 of adulthood[14,28,29]. Reversing these lipid metabolic shifts or implementing interventions at this time can effectively restore lifespan, making day 1 an essential time point for lipidomic analysis. As described above, we stained neutral lipids in fixed worms using ORO, either imaged the stained worms and quantified the staining (Fig. 1d) or extracted ORO from stained worms and estimated ORO intensity using colorimetry (Supplementary Fig. 1e). Furthermore, we used a spectroscopic assay to determine the stored TAGs (Supplementary Fig. 1f), a predominant storage lipid. Lastly, to survey the lipid composition more broadly in the different sterile mutants, we employed LC-MS (liquid chromatography-mass spectrometry) to quantify lipid species (Fig. 1e). Using these different approaches of lipid estimation, we found that the three sterile mutants accumulated significantly more lipids than WT, particularly TAGs at day 1 of adulthood (Fig. 1d, e and Supplementary Fig. 1e, f). We additionally monitored yolk proteins, which carry lipids from the pseudocoelom to the developing oocytes and represent a major source of nutrients in developing oocytes, using GFP-fused vitellogenin (VIT-2::GFP). We found that all three sterile mutants displayed higher VIT-2::GFP expression as compared to WT worms (Fig. 1f, g). In summary, despite their different lifespans, all three sterile mutants accumulated excess lipid and yolk on day 1 of adulthood.

Different types of self-sterile mutants displayed similar yet distinct lipid profiles

We next examined the lipid profiles of the three self-sterile mutants in more detail. Our LC-MS lipidomic analysis detected 1224 lipid molecules from 15 lipid groups (Fig. 2 and Supplementary Data 1). Principal Component Analysis (PCA) showed that the replicates were highly similar, supporting the high reproducibility of the data. All three sterile mutants were clearly separated from WT along PC1 (*x*-axis, Fig. 2a) and were themselves separated along PC2 (*y*-axis, Fig. 2a). As expected, the proportion of TAGs among the detected lipidome was substantially elevated in the sterile mutants compared to WT (Fig. 2b). Among the phospholipids detected, the majority were phosphatidylcholines (PCs) and phosphatidylethanolamines (PEs) (Fig. 2b). We next treated each of the 1224 detected lipid molecules as a "feature" and used the EdgeR package[30] to identify those that showed statistically significant differences between each of the sterile mutants compared to WT worms. Comparing the lipid features that showed elevated or reduced abundance among the three sterile mutants relative to WT indicated a significant overlap (Fig. 2c, d and Supplementary Data 1). We performed a lipid enrichment analysis to identify whether specific lipid classes were overrepresented among the lipids that were differentially altered in the sterile mutants. Our analysis revealed that among the elevated lipid molecules, the lipid classes TAG and PC were overrepresented; whereas for the less abundant lipid molecules, the lipid classes PE, glucosylceramides (CerG1), and phosphatidylserines (PS) were overrepresented (Fig. 2e). Interestingly, sphingosines were significantly
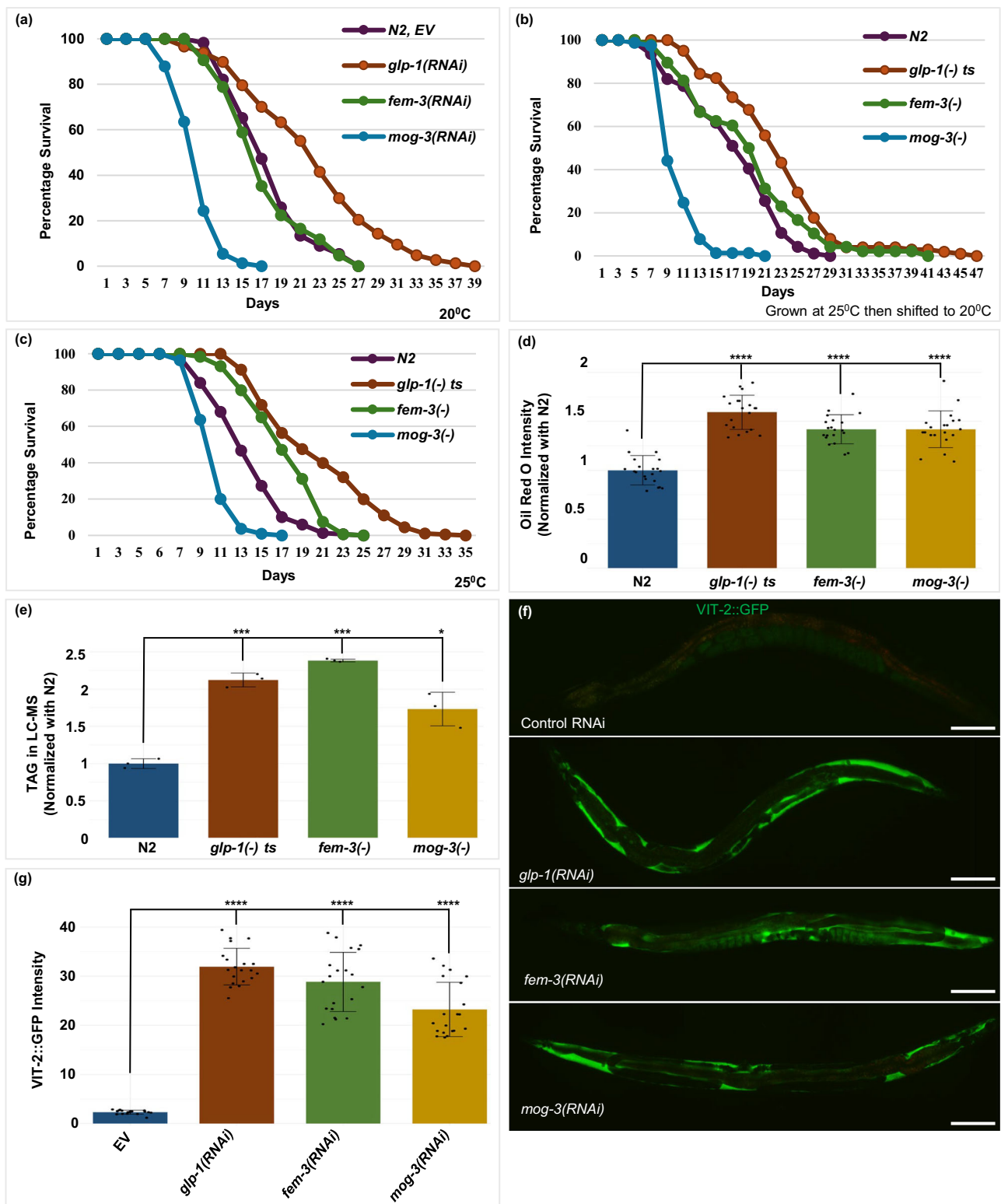
elevated in *mog-3(-)* mutants but depleted in *glp-1(-)* and *fem-3(-)* mutants (Fig. 2e).

Previous studies have implicated specific fatty acids and elevated MUFA-to-PUFA (monounsaturated fatty acids to polyunsaturated fatty acids) ratio in lifespan modulation[31–33]. We therefore examined the levels of free fatty acids in the three sterile mutants and WT worms using LC-MS. We found that the MUFA-to-PUFA ratio was higher in all three sterile mutants compared to WT regardless of their lifespan

phenotypes, but these differences did not reach statistical significance (Supplementary Fig. 2a). Similarly, the unsaturated fatty acid (UFA) to saturated fatty acid (SFA) ratio remained comparable across all groups (Supplementary Fig. 2b). In conclusion, our lipidomic analysis revealed elevated levels of TAGs and alterations in various phospholipids among the three sterile mutants at day 1 of adulthood. Additionally, distinct differences in lipid profiles were observed, particularly in a subset of sphingolipids.

Fig. 1 | Different modes of sterility induced excessive fat accumulation but differential lifespan. a Survival curves showing the lifespans (at 20 °C) of wild-type worms treated with the indicated gene RNAi at 20 °C. **b, c** Survival curves showing the lifespans of wild-type N2, *glp-1(e2144)*, *fem-3(e1996)*, and *mog-3(q74)* mutants grown at 25 °C, then aged at 20 °C (**b**), or continuously at 25 °C (**c**). The detailed mean lifespan values, the number of worms analyzed in each replicate, and statistical analyses for (**a–c**) are provided in Source Data. Two biological replicates were analyzed for each genotype. **d, e** Lipid levels estimated by Oil Red O (ORO) staining (**d**) and triacylglycerides (TAG) quantification by LC-MS, normalized to N2 (**e**), in the indicated genotypes at 25 °C. ORO intensity is shown as the means of two biological replicates per genotype, with at least 10 worms per replicate and 20 worms total per genotype. In (**d**), the *p*-values for comparisons with N2 are 8.93×10^{-14} for *glp-1(-) ts*; 9.02×10^{-11} for *fem-3(-)*, and 2.94×10^{-9} for *mog-3(-)*, respectively. In (**e**), the *p*-values for comparisons with N2 are 0.00014 for *glp-1(-) ts*;

0.00032 for *fem-3(-)*, and 0.02345 for *mog-3(-)*, respectively. TAG estimations in (**e**) are based on three biological replicates from the lipidomics LC-MS dataset. **f, g** Representative images (**f**) and quantification (**g**) of VIT-2::GFP intensity in *glp-1(RNAi)*, *fem-3(RNAi)*, and *mog-3(RNAi)* worms compared to Empty Vector (EV) RNAi controls. VIT-2::GFP intensities are shown as the mean of two biological replicates per genotype, with at least 10 worms per replicate and 20 worms total per genotype, except for *glp-1(e2144)*, for which 19 worms were analyzed. In (**g**), the *p*-values for comparisons with empty vector (EV) are 4.24×10^{-19} for *glp-1(RNAi)*; 3.63×10^{-14} for *fem-3(RNAi)*, and 5.72×10^{-13} for *mog-3(RNAi)*, respectively. In (**d**, **e**, and **g**), unpaired two-tailed Welch's *t*-tests were used to perform one-way comparisons of each genotype to empty vector (EV) RNAi control. No correction for multiple comparisons was applied. *p*-values for the tests are indicated as *p < 0.05, ***p < 0.001, ****p < 0.0001. Error bars represent standard deviations. Scale bar in (**f**), 100 μm. LC-MS - Liquid Chromatography–Mass Spectrometry.

Sterile mutants showed significant upregulation of immunity and fat metabolism genes

To understand what could contribute to the lipid and lifespan changes in the sterile mutants at the molecular level, we next compared their gene expression profiles. Previous studies have suggested that the intestine is a key site of action for several major transcription factors that mediate the germline effect on longevity[14,34,35]. Furthermore, the intestine-specific transcriptomic analysis also eliminates the difficulty in comparing strains with substantially different numbers and constituents of germ cells. We therefore carried out RNA-seq analysis using dissected intestines from the sterile *glp-1(-)*, *fem-3(-)*, and *mog-3(-)* mutant strains and compared to the WT. We again focused on day 1 of adulthood to facilitate comparison with the lipidomic data (above) and other published results. We additionally collected whole worms for RNA-seq, mainly for comparison with published data[16].

PCA of the RNA-seq data revealed substantial differences in intestinal gene expression between WT and sterile mutant strains. Interestingly, the long-lived *glp-1(-)* and *fem-3(-)* strains were separated from WT and short-lived *mog-3(-)* strains along PC1 (*x*-axis, Fig. 3a), suggesting that some gene expression differences could correlate with longevity. We also noted that *glp-1(-)* and *mog-3(-)* worms were separated from WT and *fem-3(-)* worms along PC2 (*y*-axis, Fig. 3a), suggesting that feminized mutants displayed a gene expression profile that is more similar to fully reproductive adults than to germline-less or masculinized mutants. We also applied PCA to the whole worm transcriptomic data. We found that WT and *fem-3(-)* strains grouped closely and were well separated from *glp-1(-)* and *mog-3(-)* strains on x- and y-axes, respectively (Supplementary Fig. 3a), consistent with the observation from the intestine-specific data. As a quality control, we found that our whole-worm *glp-1(-)* data were highly correlative to published data by Steinbaugh et al., 2015 (Supplementary Fig. 3b; Supplementary Data 2)[16].

We next identified the genes that showed significant gene expression changes in each of the sterile mutants compared to WT. We found 1449, 6411, and 2145 upregulated genes and 1917, 647, and 1292 downregulated genes in the intestinal datasets from *glp-1(-)*, *fem-3(-)*, and *mog-3(-)* mutant strains, respectively (Supplementary Data 3). We also compared the intestinal and whole-worm gene expression data for each of the sterile mutants. As expected, the gene expression changes detected in the intestine showed significant overlap with those in the whole-worm (Supplementary Fig. 3b–d and Supplementary Data 2).

To uncover the gene expression differences in the long-lived *glp-1(-)* and *fem-3(-)* and short-lived *mog-3(-)* mutants, we compared the significantly changed genes in each of the three genotypes. This analysis revealed several germline-enriched genes that were significantly altered in the sterile mutants (Supplementary Data 3, with germline-enriched genes highlighted in blue). We concluded that during the process of intestinal dissection, some amount of gonad must have inadvertently been associated, due to the closely linked anatomy of these two tissues[36]. We therefore filtered out germline-specific genes based on Reinke et al.

(2004)[37] and conducted differential analyses using the RNA-seq data with the germline genes removed. The analyses revealed significant overlaps among the genes that were upregulated and downregulated in the three sterile mutants (Fig. 3b, c and Supplementary Data 2). Interestingly, the masculinized *mog-3(-)* mutants showed the most substantial gene expression changes, especially for upregulated genes, whereas the *glp-1(-)* and *fem-3(-)* mutants exhibited changes that overlapped but were also distinct from the *mog-3(-)* changes (Fig. 3b, c and Supplementary Data 2). Moreover, especially among the upregulated genes, the majority of the gene expression changes in the *fem-3(-)* mutants were found within the set of changes identified in the *glp-1(-)* mutant. Gene set enrichment analysis using Wormcat[38] revealed that lipid metabolism and stress response genes were overrepresented among those that showed significant expression changes in all three sterile mutants (Fig. 3d–i and Supplementary Data 4). We further focused on the subset of significantly changed genes that are categorized as "lipid metabolism" or "stress" based on WormCat[38] and again revealed significant overlaps (Supplementary Fig. 4a–d and Supplementary Data 2). The analysis also indicated that the sterile mutants showed some unique gene expression changes, including collagen genes in *glp-1(-)* and *fem-3(-)* and transmembrane and "unassigned" genes in *mog-3(-)* (Fig. 3d–f and Supplementary Data 4).

We additionally performed clustering analysis using STRING, a network analysis tool[39], to further delineate the significantly changed lipid metabolism genes. The analysis highlighted multiple lipid metabolism pathways to be over-represented based on differentially expressed genes in the three sterile mutants (Supplementary Fig. 5a–f and Supplementary Data 5). Interestingly, sphingolipid metabolism emerged as a common pathway perturbed in the three mutants, although the number of genes in the clusters varied among the three mutants (Supplementary Fig. 5a–f and Supplementary Data 5). This finding corroborated our lipidomic analysis, indicating a subset of sphingolipids to show differential abundance among the three mutants. We additionally used MetaboAnalyst[40], an analysis tool that enables the integration of transcriptomic and lipidomic data, to gain further biological insights. The results revealed significant changes in multiple metabolic pathways (Supplementary Data 6) and, unsurprisingly, the sphingolipid metabolism pathway again emerged.

To further explore how gene expression differences may be related to sphingolipid differences, we selected the genes annotated to be involved in sphingolipid metabolism (Supplementary Fig. 5i) that were reliably detected in our RNA-seq data and performed clustering analysis. This analysis revealed that the long-lived *glp-1(-)* and *fem-3(-)* mutants cluster more closely with each than with *mog-3(-)* mutants (Supplementary Fig. 5g, Source Data), supporting a shared mechanism of altered sphingolipid metabolism between the long-lived *glp-1(-)* and *fem-3(-)* mutants that is divergent from that in the *mog-3(-)* mutant. In particular, genes in clusters 2 and 3 of Supplementary Fig. 5g showed opposing expression trends. We came to a similar conclusion when the clustering analysis was performed using genes in the sphingolipid
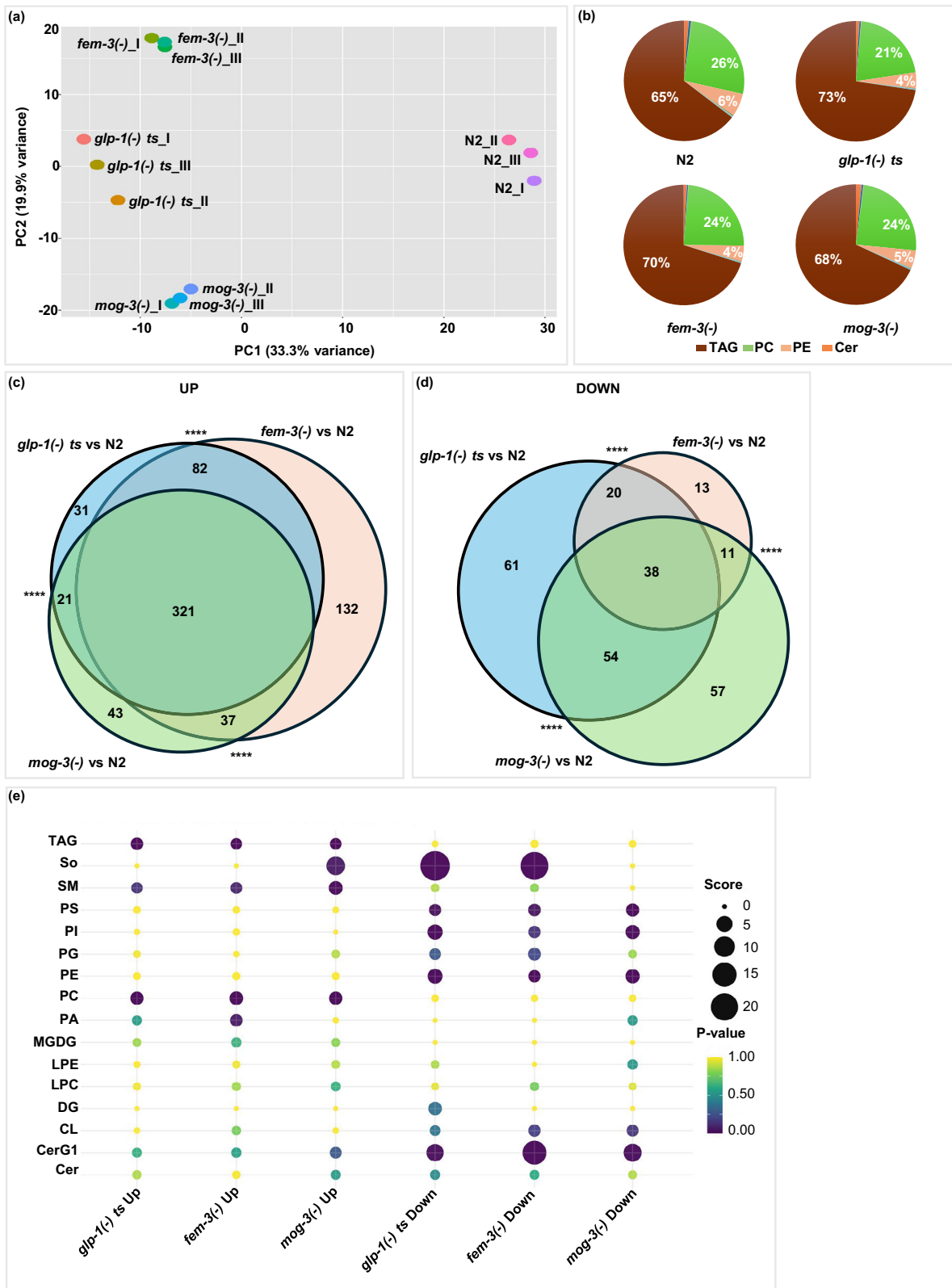
metabolism pathway that were significantly altered in at least one genotype (Supplementary Fig. 5h, Source Data), where cluster 3 shows opposing expression trends. These differences provide a plausible transcriptional explanation for the divergent sphingosine levels observed among the mutants. However, at this level of analysis, it is difficult to know exactly how the opposing expression patterns of these particular enzymes between the long-lived *glp-1(-)* and *fem-3(-)*

mutants and the short-lived *mog-3(-)* mutant result in the intriguing difference in sphingosine levels among the three mutants.

Among the stress response genes that were significantly changed in the three sterile mutants, pathogen/innate immune genes were particularly overrepresented (Fig. 3). We further compared the upregulated genes that were annotated as pathogen-responsive (based on WormCat[38]) among the three sterile mutants and observed a

Fig. 2 | Lipidomic analyses revealed that the different sterile mutant strains share similar but also distinct lipid profiles. a Principal Component Analysis (PCA) analysis of three replicates of wild-type N2, *glp-1(e2144)*, *fem-3(e1996)*, and *mog-3(q74)* showed that the mutants are clearly separated from wild-type N2. Each dot indicates one replicate. PCA plot was generated using R. **b** Relative distribution of different lipids in N2, *glp-1(e2144)*, *fem-3(e1996)*, and *mog-3(q74)* worms showed that the major portions of the lipidome were comprised of TAG, PC, and PE and Sphingolipids, especially Ceramides. **c, d** Venn diagram showing upregulated lipid molecules (**c**) and downregulated lipid molecules (**d**) in *glp-1(e2144)*, *fem-3(e1996)*, and *mog-3(q74)* vs N2. Detailed lists of lipid molecules are provided in Supplementary Data 1. Fisher's exact

test was used to assess the significance of overlaps. **** indicates *p*-value < 0.0001. **e** Bubble plot showing lipid enrichment analysis. Circle diameter represents the enrichment score, while color intensity corresponds to the *p*-value. Statistical significance was assessed using one-sided Fisher's exact test, without correction for multiple comparisons. See Supplementary Methods for details. PA Phosphatidic acid, CerG1 Glucosylceramide, TAG Triacylglyceride, SM Sphingomyelin, PC Phosphatidylcholine, PE Phosphatidylethanolamine, Cer Ceramide, LPC Lysophosphatidylcholine, MGDG Monogalactosyldiacylglycerol, PI Phosphatidylinositol, CL Cardiolipin, PS Phosphatidylserine, LPE Lysophosphatidylethanolamine, PG Phosphatidylglycerol, DG Diacylglycerol, So Sphingosine.

---

significant overlap, where the changes in *fem-3(-)* represented a subset of those changed in *glp-1(-)* mutant (Supplementary Fig. 6a and Supplementary Data 2), and *glp-1(-)* and *mog-3(-)* mutants shared ~half of the significantly changed genes. These data prompted us to examine the immunity phenotype of the three sterile mutants. We employed the well-established model of *Pseudomonas aeruginosa (PA14)* infection[41] and found that all three mutants survived better upon PA14 infection compared to WT worms (Supplementary Fig. 6b; Source Data), even when PA14 infection was initiated in post-reproductive adults.

The lifespans of different sterile mutants are dependent on distinct genetic pathways known to contribute to longevity

We next investigated whether the genes exhibiting differential expressions in *glp-1(-)*, *fem-3(-)*, and *mog-3(-)* mutants shared enrichment of any specific transcription factor binding motif, which would suggest putative transcriptional regulators. Motif analysis using the MEME[42] revealed a notable enrichment of DAF-16 binding motif among the genes differentially expressed in *glp-1(-)* and *fem-3(-)* worms; conversely, the genes that exhibited altered expression in *mog-3(-)* mutant did not display a similar enrichment for DAF-16 motifs (Supplementary Data 7). This contrast suggested that the lifespan extension observed in *glp-1(-)* and *fem-3(-)* worms is closely linked to DAF-16 activation, a connection absent in *mog-3(-)* worms.

DAF-16/FOXO is a key downstream transcription factor of insulin/IGF-1 signaling pathway and has been implicated in several longevity-affecting regimens, including lifespan extension mediated by germline loss[6,43–45]. Upon germline removal, DAF-16/FOXO enters the intestinal nuclei and regulates downstream target genes[6]. We tested the effects of *daf-16* removal in wild-type, *glp-1(-)*, *fem-3(-)*, and *mog-3(-)* mutant strains. Under our experimental condition (25 °C), *daf-16* RNAi completely suppressed the extended lifespan of the *glp-1(-)* and *fem-3(-)* worms but did not significantly alter the already shortened lifespan of the *mog-3(-)* mutant (Fig. 4a and Supplementary Fig. 7a; Source Data). We also examined DAF-16::GFP subcellular localization in the intestinal cells of the various strains, as previous studies showed that DAF-16::GFP is localized to the nucleus of the germline-less worms[34]. We found that most of the *glp-1(-)* worms showed nuclear DAF-16::GFP, as did *fem-3(-)* worms; in contrast, DAF-16::GFP remained cytoplasmic in *mog-3(-)* worms (Fig. 4c, d). We additionally confirmed these results using SOD-3::GFP, a reporter of DAF-16 activation[46]. As expected, *glp-1(-)* worms displayed increased SOD-3::GFP intensity[47]. Interestingly, we found that *fem-3(-)* worms also showed higher induction of SOD-3::GFP, whereas *mog-3(-)* worms did not display any change in SOD-3::GFP intensity (Supplementary Fig. 7b, c). We further performed a time-course experiment to assess the timing of DAF-16 activation. We found that DAF-16::GFP localized to intestinal nuclei in *glp-1(-)* and *fem-3(-)* worms starting at day 1 of adulthood (1 DA) and persisted to day 12 of adulthood (12 DA) (Fig. 5a). In contrast, *mog-3(-)* worms showed slight nuclear localization of DAF-16::GFP in day 1 adult worms but not at the other time points examined (Fig. 5a). Interestingly, we found that DAF-16 became nuclear starting in day 5 of adulthood in WT worms and remained nuclear at the last time point (Fig. 5a), consistent with previous findings[48]. Overall, our data are consistent with the possibility

that persistent activation of DAF-16 starting on day 1 of adulthood could be essential for lifespan extension.

As we demonstrated that the lifespan of *glp-1(-)* and *fem-3(-)* worms is contingent upon DAF-16 activation, we explored whether ectopically activating DAF-16 in *mog-3(-)* worms could extend their lifespan. DAF-16 is well established to be translocated into the nucleus and become activated when *daf-2*, which encodes the insulin-like receptor in *C. elegans*, is inhibited. We therefore applied *daf-2* RNAi to both *mog-3(-)* mutants and *mog-3(-)* mutants expressing DAF-16::GFP as a way to ectopically activate DAF-16. Our studies indicated that DAF-16::GFP relocated to the nucleus following *daf-2* RNAi treatment, indicative of ectopic activation of DAF-16 (Supplementary Fig. 8a–e). Moreover, we found that *daf-2* RNAi treatment effectively prolonged the lifespan of *mog-3(-)* mutants (Supplementary Fig. 8f, Source Data). These results suggested that enhancing DAF-16 activity can increase the lifespan of the short-lived *mog-3(-)* worms.

Excess fat and yolk have been suggested to activate the transcription factor SKN-1/Nrf2[16], which has been shown to promote lifespan in germline-less mutants[49,50]. Since the three sterile mutants accumulated elevated lipid and vitellogenin levels (Fig. 1 and Supplementary Fig. 1), we examined whether their lifespan extension depends on SKN-1 function. We found that the lifespans of all four strains (WT, *glp-1(-)*, *fem-3(-)*, and *mog-3(-)*) were decreased upon depletion of *skn-1* (Fig. 4b and Supplementary Fig. 7a, Source Data). The degree of lifespan reduction was greatest in the *glp-1(-)* mutant, and least in the short-lived *mog-3(-)* mutant (Supplementary Fig. 7a; Source Data). We additionally used GST-4::GFP as a reporter of SKN-1 activity[51]. We found that *glp-1(-)* worms displayed increased GST-4::GFP intensity as expected; interestingly, *fem-3(-)* and *mog-3(-)* worms also showed increased expression of GST-4::GFP (Fig. 4e, f). We additionally used GST-4::GFP to monitor SKN-1 activation over time in the three sterile mutants. We observed the onset of GST-4::GFP induction at the L4 stage, which persisted until day 7 of adulthood, with peak elevation in day 1 adults in all the strains tested (Fig. 5b). The temporal induction of GST-4::GFP was greater in the sterile mutants compared to WT, consistent with the notion that these mutants harbor elevated levels of lipid, which result in GST-4 induction. Overall, these results indicate that SKN-1 is activated in all three sterile mutants and appears to be a key regulator of their lifespan, but is not the factor that accounts for their differential lifespan.

DAF-16 and SKN-1 activation in long-lived *glp-1(-)* and *fem-3(-)* are differentially dependent on accumulated fat

Previous studies have suggested that altered fat levels could induce longevity-promoting factors[12,14]. Therefore, we investigated the roles of fat accumulation on DAF-16 and SKN-1 activation in the three sterile mutants. FAT-6 and FAT-7 encode fatty acid desaturases and are key enzymes for the production of MUFAs and overall fat storage. Since *fat-6* and *fat-7* share significant sequence homology, both genes are effectively knocked down by *fat-6* RNAi. We found that nuclear accumulation of DAF-16::GFP was partially but significantly rescued in *glp-1(-)* and *fem-3(-)* worms upon RNAi depletion of *fat-6/fat-7*. Nuclear DAF-16::GFP was detected in ~40% and ~23% of the worms in *fat-6* RNAi-treated *glp-1(-)* and *fem-3(-)* worms, respectively, compared to ~90% in control RNAi-treated worms (Supplementary Figs. 9a and 10).
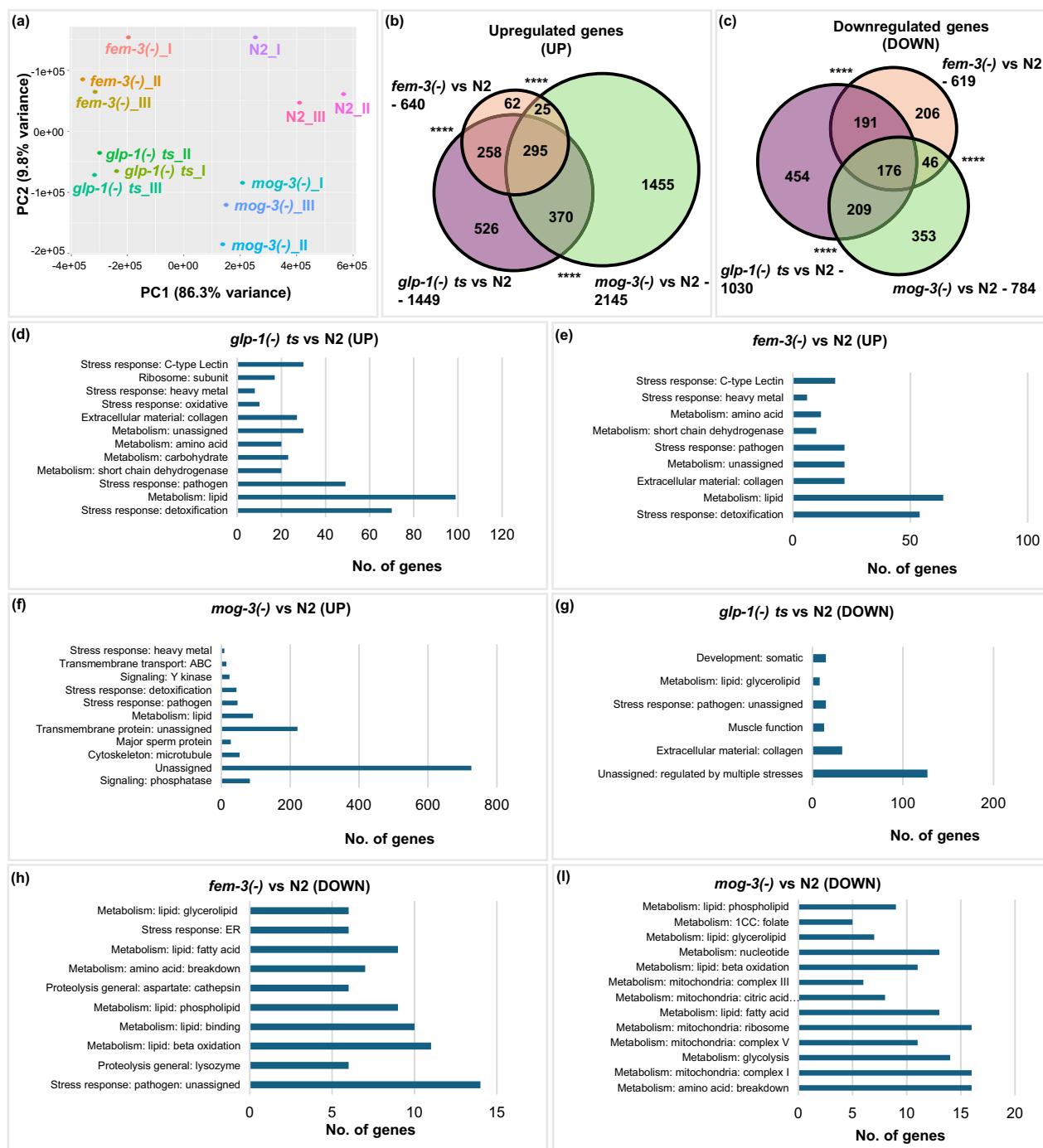
Fig. 3 | Intestinal-specific transcriptomic analyses revealed that the sterile mutants showed significant upregulation of immunity and fat metabolism genes. a Principal component analysis (PCA) analysis of RNA-seq data for three replicates of N2, *glp-1(e2144)*, *fem-3(e1996)*, and *mog-3(q74)* worms showed that the long-lived *glp-1(e2144)* and *fem-3(e1996)* worms are clearly separated from wild-type N2 and short-lived *mog-3(-)* worms. Each dot indicates one replicate. PCA plot was generated using R. Dissected intestines at the young adult stage were used to generate the RNA-seq data. **b** The Venn diagram illustrates substantial overlaps among upregulated genes (UP) in *glp-1(e2144)*, *fem-3(e1996)*, and *mog-3(q74)* mutants, in comparison to N2. Notably, the number of upregulated genes in *glp-1(e2144)*, *fem-3(e1996)*, and *mog-3(q74)* mutants are 1449, 640, and 2145, respectively, with 295 genes being commonly upregulated across all three mutants. **c** The Venn diagram illustrates substantial overlaps among downregulated genes (DOWN) in *glp-1(e2144)*, *fem-3(e1996)*, and *mog-3(q74)* mutants, in comparison to N2. Notably, the number of downregulated genes in *glp-1(e2144)*, *fem-3(e1996)*, and

mog-3(q74) mutants are 1030, 619, and 784, respectively, with 176 genes being commonly downregulated across all three mutants. Additionally, significant overlaps were observed in pairwise comparisons of up and downregulated genes among these mutants. The gene lists and overlaps shown in (**b** and **c**) are shown in Supplementary Data 2. Fisher's exact test was used to assess the significance of overlaps. **** indicates *p*-value < 0.0001. **d–f** Gene set enrichment analysis showed that metabolism and stress response genes are among the common categories that are over-represented in the upregulated genes (UP) in *glp-1(e2144)* (**d**), *fem-3(e1996)* (**e**), and *mog-3(q74)* (**f**), relative to N2. Detailed category lists are provided in Supplementary Data 4. **g–i** Gene set enrichment analysis revealed that lipid metabolism and stress response genes are commonly overrepresented among the downregulated genes (DOWN) in *glp-1(e2144)* (**g**), *fem-3(e1996)* (**h**), and *mog-3(q74)* (**i**) mutants, compared to N2. Furthermore, collagen genes and mitochondrial metabolism are specifically over-represented in *glp-1(e2144)* and *mog-3(q74)* mutants, respectively. Detailed category lists are shown in Supplementary Data 4.
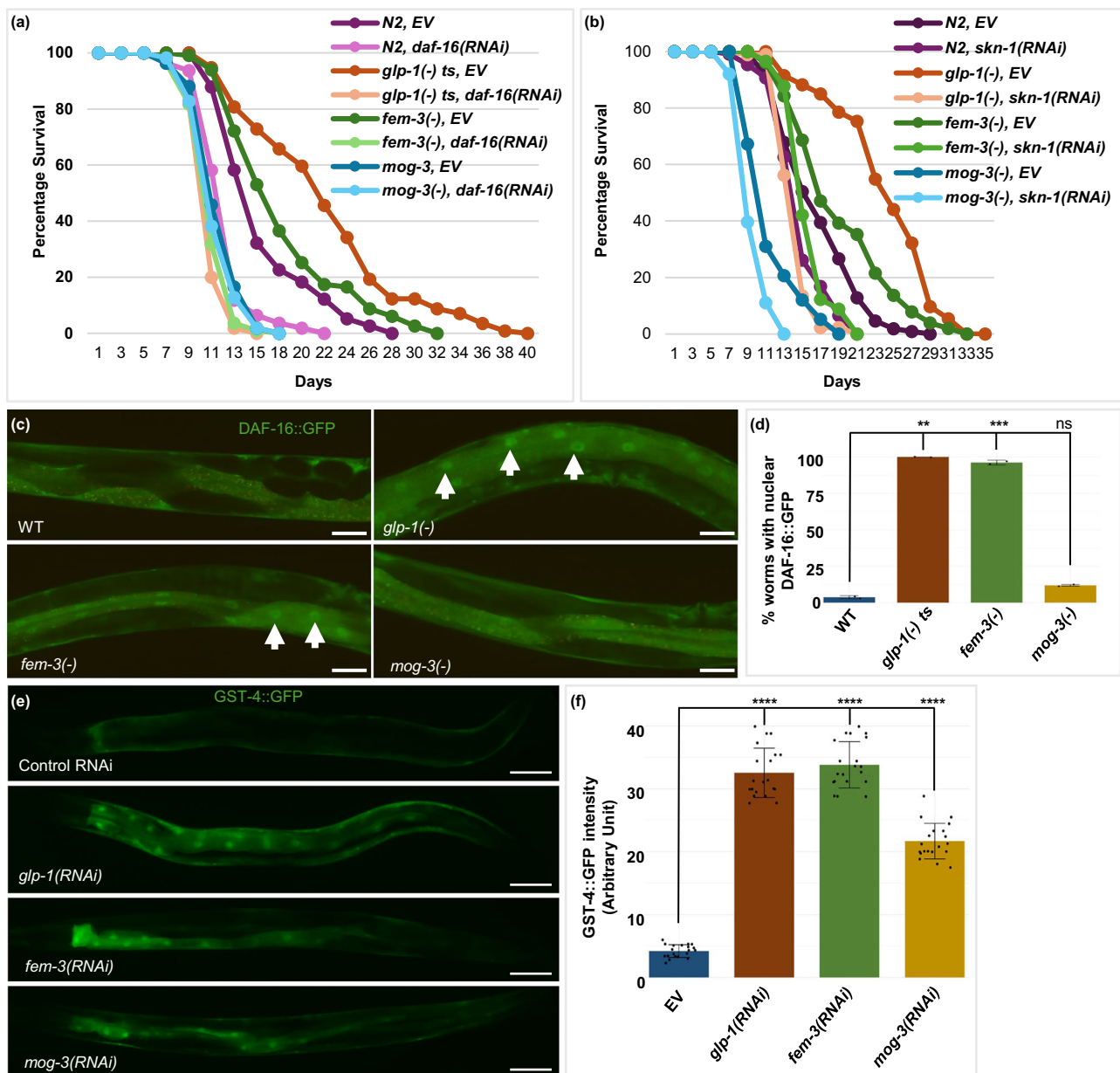
Fig. 4 | The lifespans of different sterile mutants were dependent on distinct genetic pathways. a, **b** Survival curves showing the lifespans of wild-type N2, *glp-1(e2144)*, *fem-3(e1996)*, and *mog-3(q74)* worms upon *daf-16* (**a**), and *skn-1* RNAi (**b**). Two biological replicates were analyzed for each genotype. The detailed mean lifespan values, the number of worms analyzed in each replicate, and statistical analyses for (**a** and **b**) are provided in Source Data. **c**, **d** Representative images (**c**) and quantification (**d**) demonstrate pronounced nuclear localization of DAF-16::GFP in *glp-1(RNAi)* and *fem-3(RNAi)* worms, contrasting with the absence of such localization in *mog-3(RNAi)* worms. The *y*-axis depicts the mean percentage of worms exhibiting nuclear GFP localization, based on two biological replicates per genotype, with at least 30 worms per replicate. The total number of worms analyzed per genotype was 76 (WT, control); 79 [*glp-1(-) ts*]; 68 [*fem-3(-)*], and 77 [*mog-3(-)*]. Arrowheads mark nuclear DAF-16::GFP. In (**d**), the *p*-values for comparisons with WT control are 0.0049 for *glp-1(-) ts*; 0.00059 for *fem-3(-)*, and 0.1298 for *mog-*

3(-), respectively. Scale bar in **c**, 50 μm; in **e**, 100 μm. **e**, **f** Representative images (**e**) and their quantifications (**f**) showed that *gst-4::gfp* is elevated in *glp-1(RNAi)*, *fem-3(RNAi)*, and *mog-3(RNAi)* worms. *y*-axis represents mean GST-4::GFP intensities of two biological replicates per genotype, with at least 10 worms per replicate and 20 worms total per genotype. In (**f**), the *p*-values for comparisons with empty vector (EV) RNAi control are 2.01×10^{-19} for *glp-1(RNAi)*; 1.29×10^{-20} for *fem-3(RNAi)*, and 5.60×10^{-19} for *mog-3(RNAi)*, respectively. In (**d**), data were analyzed using an independent two-sample *t*-test. In (**d** and **f**), unpaired two-tailed Welch's *t*-tests were used to perform one-way comparisons of each genotype to empty vector (EV) RNAi control. No correction for multiple comparisons was applied. Statistical significance was set at $p < 0.05$. *p*-values for the tests are indicated as **$p < 0.01$, ***$p < 0.001$, ****$p < 0.0001$, and ns for not significant. Error bars represent standard deviations.

Interestingly, fat depletion completely reversed the intestinal expression of GST-4::GFP in all sterile worms, including the faint expression in WT worms (Supplementary Figs. 9b and 11). In parallel, we administered *fat-6* RNAi to WT, *glp-1(-)*, *fem-3(-)*, and *mog-3(-)* worms to verify the effectiveness of the RNAi treatment on *fat-6*. Our observations confirmed that *fat-6* RNAi notably reduced the ORO staining across all

these worm types (Supplementary Fig. 12). The results indicated that excess fat storage is key to intestinal SKN-1 activation in the strains tested, irrespective of their lifespan phenotype. Furthermore, DAF-16 activation was partially dependent on fat storage, but additional factors likely also contribute to DAF-16 activation in *glp-1(-)* and *fem-3(-)* mutants, which mediates their extended lifespan.
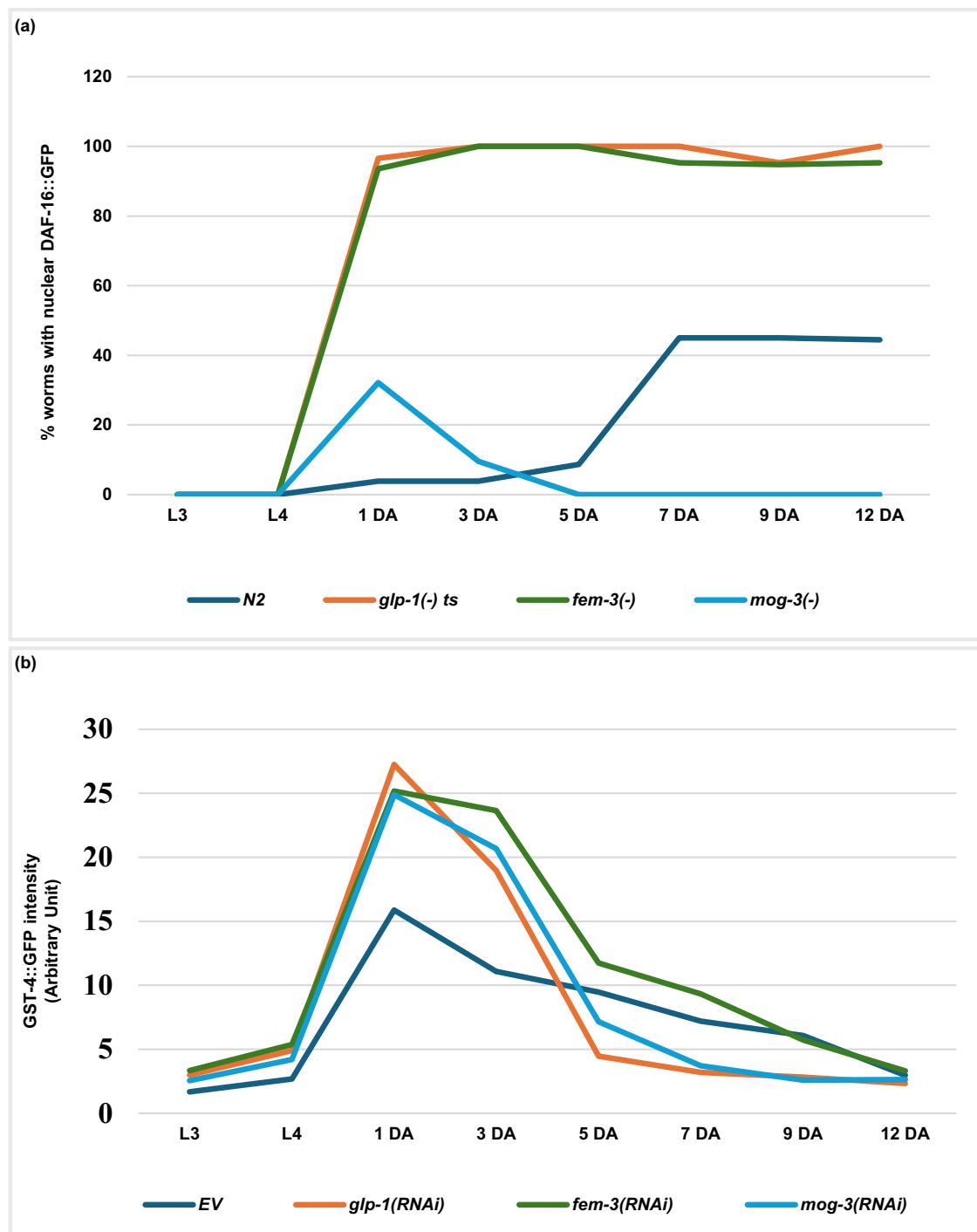
Fig. 5 | Time course analysis of DAF-16 and SKN-1 activation. a Percentage of wild-type N2, *glp-1(e2144)*, *fem-3(e1996)*, and *mog-3(q74)* worms with nuclear DAF-16::GFP at 8 different stages of their lives as described previously. **b** GST-4::GFP signal intensity in wild-type worms treated with the indicated RNAi at 8 different stages of their lives, including two larval stages (L3 and L4), two reproductive stages (day 1 and day 3 of adulthood, 1 DA and 3 DA), and four post-reproductive stages (5 DA, 7 DA, 9 DA, 12 DA). EV, Empty vector RNAi. For (**a**), the mean percentage of worms exhibiting nuclear DAF-16::GFP localization is shown, based on two biological replicates per genotype, with at least 30 worms per replicate. The total number of worms analyzed per genotype was: 82 (N2, control), 89 [*glp-1(-)*], 74 [*fem-3(-)*], and 69 [*mog-3(-)*]. For (**b**), GST-4::GFP intensities from two biological replicates per genotype are shown, with at least 7 worms per replicate and 15 worms total per genotype. These experiments were performed at 25 °C.

Excess sperm production and continuous germline proliferation shorten lifespan in MOG worms

We next wondered what might contribute to the shortened lifespan of the *mog-3(-)* mutant. Masculinized mutants lack male somatic tissues, but they produce a large number of sperm[26], substantially greater than the ~300 sperm typically produced by hermaphrodites. We

investigated whether excessive sperm production could compromise their lifespan. To test this, we treated *mog-3(-)* worms with *spe-26* RNAi and examined their lifespan. SPE-26 is predicted to have actin-binding activity and is expressed in spermatocytes[52]. Loss of *spe-26* results in defective spermatocyte production and loss of mature spermatids and functional sperm[52]. We found that RNAi depletion of *spe-26* decreased
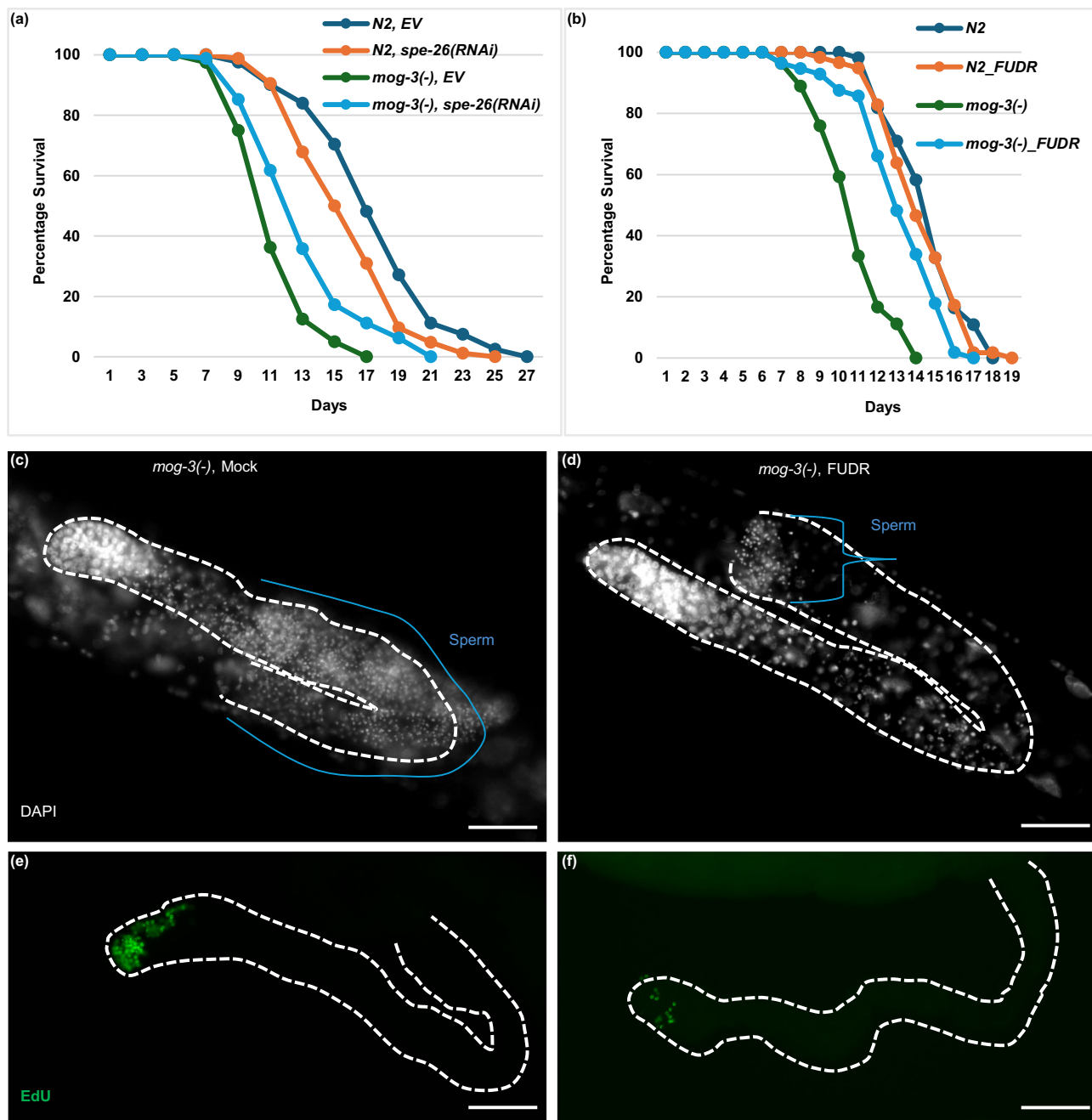
Fig. 6 | Excess sperm production and continuous germline proliferation shorten lifespan in *mog-3(-)* worms. a Survival curves showing the lifespans of wild-type N2 and *mog-3(q74)* worms upon *spe-26* RNAi. **b** Survival curves showing the lifespans of wild-type N2 and *mog-3(q74)* worms upon FUDR treatment. In (**a** and **b**), two biological replicates were analyzed for each genotype. The detailed mean lifespan values, the number of worms analyzed in each replicate, and statistical analysis for (**a** and **b**) are provided in Source Data. **c**, **d** Representative DAPI-stained images of whole worms in *mog-3(q74)* upon mock (**c**) and FUDR treatment (**d**). **e**, **f** Representative EdU -stained images of dissected gonads in *mog-3(q74)* upon mock (**e**) and FUDR treatment (**f**). Scale bars in (**c**–**f**), 50 μm. FUDR 5-Fluoro-2′-deoxyuridine; DAPI 4′,6-diamidino-2-phenylindole; EdU 5-ethynyl-2′-deoxyuridine.

the lifespan of wild-type worms but significantly increased the lifespan of *mog-3(-)* mutants (Fig. 6a, Source Data). This finding suggested that the production of excess sperm shortens the lifespan of *mog-3(-)* mutants. We sought another way to halt sperm production; we treated *mog-3(-)* worms with low-dose (50 μM) of 5′-fluorodeoxyuridine (FUdR), a DNA synthesis inhibitor that suppresses germ cell proliferation[53]. As expected, FUdR treatment reduced sperm production, as confirmed by DAPI staining (Fig. 6c, d), and decreased germline proliferation, evidenced by a reduction in EdU-positive nuclei (Fig. 6e, f). Excitingly, we found that FUdR treatment largely rescued the shortened lifespan of *mog-3(-)* mutants (Fig. 6b, Source Data). We note

that strong inhibition of germline proliferation is well known to extend *C. elegans* lifespan[6], like the *glp-1(-)* mutant, but our low-dose FUdR treatment condition did not affect WT lifespan. Taken together, the results suggested that high levels of germline proliferation and production of a large number of sperm have a substantially negative impact on the lifespan of masculinized *mog-3(-)* worms.

MOG worms mimic male/mating-induced demise (MID)
We next wondered why the production of excessive number of sperm appears detrimental to *mog-3(-)* mutants, but sperm production per se does not compromise the lifespan of male worms[54]. We wondered
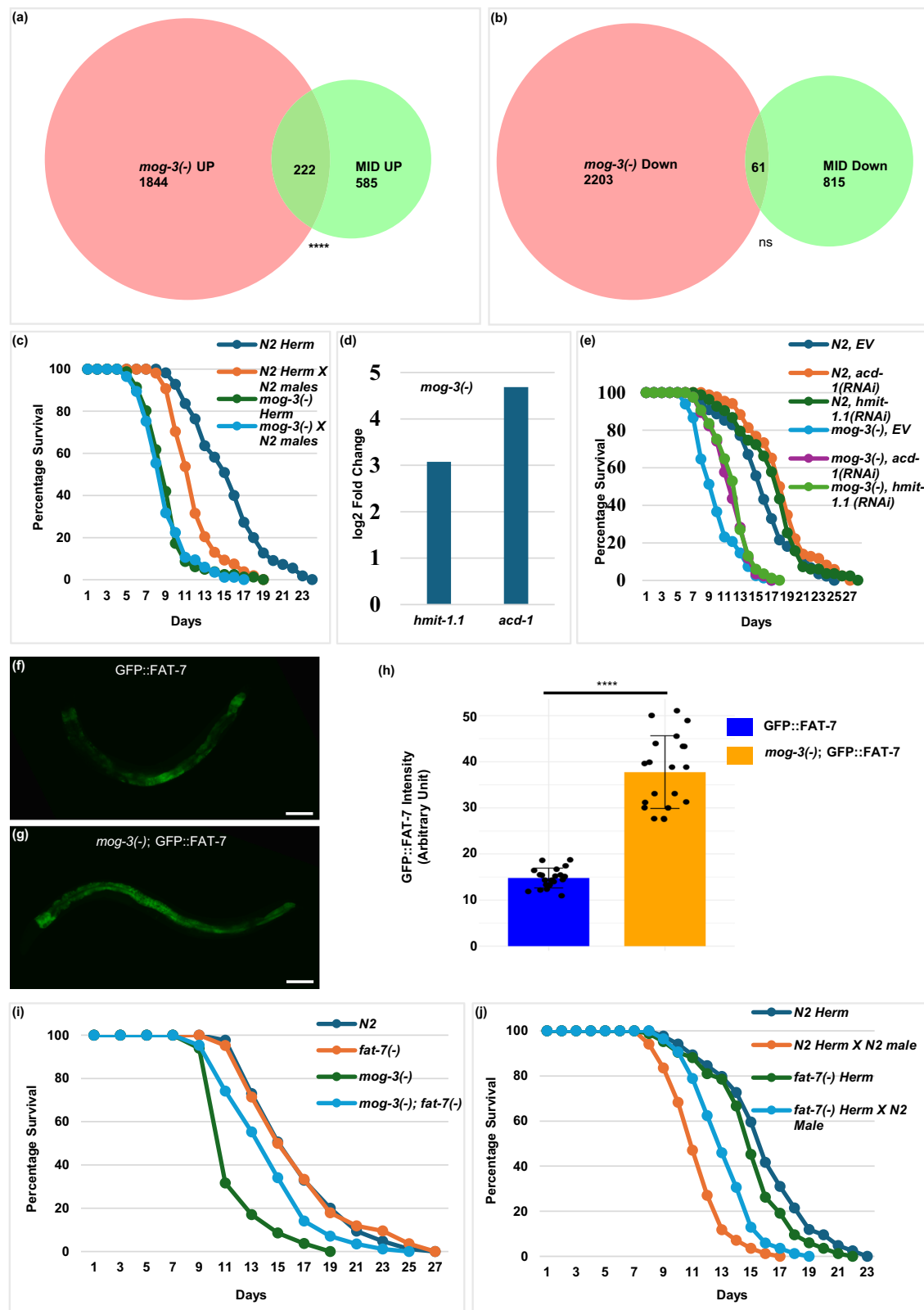
whether MOG mutants may partially resemble the physiological state of mated hermaphrodites, as MOG mutants produce excess sperm but appear to retain hermaphroditic soma[55,56]. Interestingly, mating with males have been well-documented to impose significant physiological costs on hermaphrodites and to result in drastically shortened lifespan, known as male/mating-induced demise (MID)[57,58]. We therefore compared the transcriptomes of *mog-3(-)* and another MOG mutant,

fem-3(gf) (gain-of-function mutation), with that of mated hermaphrodites[21]. This comparison revealed a significant overlap between the upregulated genes (Fig. 7a, Supplementary Fig. 13b, and Supplementary Data 2), although many unique gene expression changes specific to *mog-3(-)* and *fem-3(gf)* mutants or mated WT hermaphrodites were also evident, which are to be expected due to the different experimental conditions in separate studies. In the

Fig. 7 | MOG worms exhibit a mating/male-induced demise (MID)-like phenotype. a, b Venn diagrams showing significant overlaps between the upregulated genes in *mog-3(q74)* and genes upregulated in mated worms (**a**) and downregulated genes in *mog-3(q74)* and genes downregulated in mated worms[21]. A detailed list of genes is provided in Supplementary Data 2. Fisher's exact test was used to assess the significance of overlaps in (**b**–**d**). **** indicates *p*-value < 0.0001, ns not significant. **c** Survival curves showing the lifespans of wild-type N2 and *mog-3(q74)* worms upon mating with N2 males. **d** log2 fold Change of the indicated genes from whole-worms RNA-seq in *mog-3(q74)* worms. **e** Survival curves showing the lifespans of wild-type N2 and *mog-3(q74)* worms upon *acd-1* and *hmit-1.1* RNAi. **f**–**h** Representative images of GFP::FAT-7 expression in wild-type (**f**) and *mog-3(q74)*; GFP::FAT-7 (**g**) worms, with quantification of GFP intensity shown in (**h**). The *y*-axis represents the mean GFP intensity from two independent replicates. The *y*-axis represents the mean GFP::FAT-7 intensity from two biological replicates per genotype, with at least 10 worms per replicate and 20 worms total per genotype. In (**h**), the *p*-values for the comparison between GFP::FAT-7 and *mog-3(-)*; GFP::FAT-7 is 1.88×10^{-11}. In (**h**), unpaired two-tailed Welch's *t*-tests were used for all pairwise comparisons. No correction for multiple comparisons was applied. Statistical significance was set at *p* < 0.05. *p*-values for the tests are indicated as *p < 0.05, **p < 0.01, ***p < 0.001, and ns for not significant. Error bars represent standard deviations. Scale bars in (**f**) and (**g**), 100 μm. **i** Survival curves showing the lifespans of wild-type N2, *fat-7(wa36)*, *mog-3(q74)*, and *mog-3(q74), fat-7(wa36)*. **j** Survival curves showing the lifespans of wild-type N2 and *fat-7(wa36)* worms upon mating with N2 males. In (**c**, **e**, **i**, and **j**), two biological replicates were analyzed for each genotype. The detailed mean lifespan values, the number of worms analyzed in each replicate, and statistical analysis are provided in Source Data. EV empty vector RNAi.

downregulated genes as well, some overlap was observed, although it did not reach statistical significance. (Fig. 7b, Supplementary Fig. 13b, and Supplementary Data 2). This finding provides molecular evidence that *mog* mutants partially mimic mated hermaphrodites, and supports our hypothesis that the shortened lifespan of *mog* mutants resemble MID.

Given that pathways associated with MID may already be active in *mog-3(-)* worms, we investigated how mating with wild-type males affected the *mog-3(-)* mutants compared to WT. As expected, we observed that the lifespan of WT hermaphrodites was significantly reduced upon mating (Fig. 7c, Source Data). Interestingly, the lifespan of *mog-3(-)* worms showed no significant change after mating (Fig. 7c, Source Data). We interpreted these results to suggest that MID pathways are already active in *mog-3(-)* worms, and therefore, additional mating does not further reduce their lifespan. We additionally monitored germline proliferation as the literature indicates that mated hermaphrodites exhibit enhanced germline proliferation[58]. Using EdU labeling with a 24-h chase, we observed sustained EdU signal beyond S-phase, indicating enhanced progression through the cell cycle in *mog-3(-)* mutants (Supplementary Fig. 14a–d). Furthermore, we observed that mid-life *mog-3(-)* mutants exhibited a progressive decline in intestinal structural integrity (Supplementary Fig. 14h–j), reminiscent of the intestinal degeneration previously observed in mated hermaphrodites[57].

Thus far, we have demonstrated that *mog-3(-)* mutants resemble mated hermaphrodites based on several phenotypic assays and transcriptomic comparisons. However, unlike mated hermaphrodites, *mog-3(-)* mutants retain higher levels of fat. We hypothesized that lipid retention in *mog-3(-)* mutants is likely due to the lack of embryo production. To test this, we mated feminized *fem-3(-)* worms with either *him-5(-)* males (normal) or sperm-defective *mab-3(-); him-5(-)* males. Only worms mated with *him-5(-)* males showed pronounced fat loss based on ORO staining, supporting embryo production as a major driver of mating-induced fat depletion and explaining the discrepancy in fat levels between *mog-3(-)* and mated hermaphrodites (Supplementary Fig. 14e–g).

We next focused on the genes previously implicated to be involved in MID[21]. Among these candidate genes, we identified several that were upregulated in *mog-3(-)* worms based on our transcriptomic analysis, similar to those in mated hermaphrodites[21]. These genes include *acd-1*, encoding an acid-sensitive degenerin, and *hmit-1.1*, encoding a myoinositol transporter (Fig. 7d). Previous studies have indicated that knockdown of *acd-1* and *hmit-1.1* confers partial resistance to MID[21]. We conducted RNAi knockdown of *acd-1* and *hmit-1.1* in *mog-3(-)* mutants and found that RNAi depletion of either gene significantly extended their lifespan (Fig. 7e, Source Data), suggesting that increased expression of *acd-1* and *hmit-1.1* in the *mog-3(-)* mutants contributes to their shortened lifespan. This finding further supports the resemblance between the shortened lifespan of MOG mutants and the MID phenotype.

We noted an additional interesting gene *fat-7*, which encodes a Δ9 fatty acid desaturase, that usually acts alongside its paralog *fat-6*. Unexpectedly, *fat-7*, but not *fat-6*, is uniquely upregulated in *mog-3(-)* mutants, as well as in mated hermaphrodites[21]. In addition to expression change[21], the downstream product of FAT-7 activity, oleic acid, has been shown to rescue MID[59]. To more thoroughly test the involvement of *fat-7* in *mog-3(-)* lifespan, we additionally examined the expression level of *gfp::fat-7*, a translational fusion reporter strain. In comparison to wild-type (WT) worms, *mog-3(-)* worms exhibited increased GFP::FAT-7 levels, indicating that the FAT-7 fusion protein is indeed upregulated in *mog-3(-)* worms (Fig. 7f–h). To investigate the role of FAT-7 in the lifespan phenotype of *mog-3(-)* worms, we generated *mog-3(-); fat-7(-)* double mutants and assessed their lifespan. We found that the double mutants lived significantly longer than the single *mog-3(-)* mutants (Fig. 7i, Source Data). To further explore whether *fat-7(-)* mutants are themselves resistant to MID, we mated these worms with WT (N2) males and scored their lifespan. Interestingly, we found that *fat-7(-)* mutants exhibited partial resistance to MID (Fig. 7j, Source Data). This observation suggested that elevated *fat-7* expression contributes to the early demise of mated hermaphrodites and *mog-3(-)* mutant, further supporting the idea that the shortened lifespan of *mog-3(-)* mutants resembles the MID phenotype.

Hermaphrodites defective in sensory processing of male signals, such as *che-13* mutants, show partial resistance to MID[57]. Since *mog* worms exhibit metabolic similarities to males[56], we hypothesized that *mog-3(-)* mutants synthesize male-like metabolites that they in turn sense, which then activate genes and pathways that shorten lifespan. In support of this hypothesis, we found that *che-13* was overexpressed in *mog-3(-)* worms (Fig. 8a). If this upregulation of *che-13* contributes to the lifespan reduction in *mog-3(-)* worms, we predicted that *mog-3(-); che-13(-)* double mutants would display a rescue of lifespan. Strikingly, *mog-3(-); che-13(-)* double mutants lived significantly longer than the single *mog-3(-)* mutants and in fact, their lifespan was largely restored to that of WT worms (Fig. 8b, Source Data).

This finding was exciting and indicated that sensory perception and processing could be a major conduit that causes MOG worms to exhibit drastically shortened lifespan. Together, our results indicated that the shortened lifespan of *mog-3(-)* worms require the same genetic components that also mediate MID, supporting shared molecular mechanisms that drive lifespan reduction in MOG worms and during MID.

Discussion

In this study, we used *C. elegans* models of self-sterility to better understand the connection between reproduction, fat metabolism, and longevity. Our results revealed that different genetic disruptions that cause self-sterility result in the accumulation of excess lipids, but defective proliferation of germline stem cells leads to the most robust lifespan extension, in agreement with a relationship gleaned from previous studies[6]. We uncovered that feminization of the germline
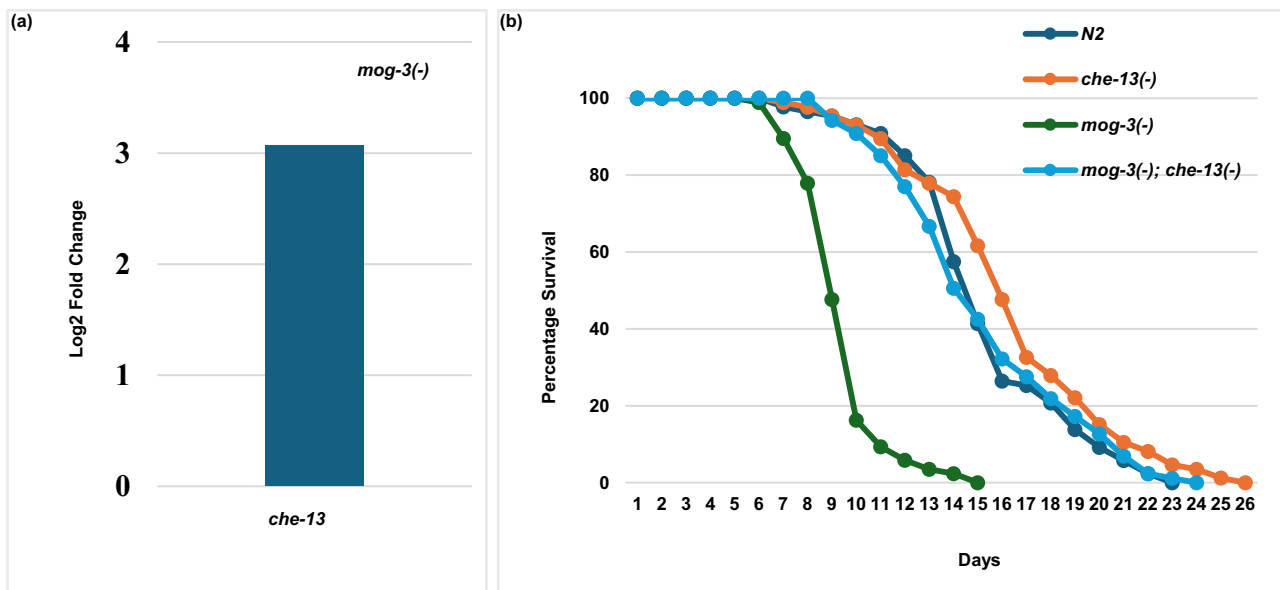
Fig. 8 | Male pheromone sensing is overactivated in masculinized worms, contributing to mating/male-induced demise (MID)-like phenotype. a log2 fold Change of *che-13* from whole-worm RNA-seq in *mog-3(q74)* worms. **b** Survival curves showing the lifespans of wild-type N2, *che-13(e1805)*, *mog-3(q74)* and *mog-3(q74); che-13(e1805)*. Two biological replicates were analyzed for each genotype. The detailed mean lifespan values, the number of worms analyzed in each replicate, and statistical analyses for (**b**) are provided in Source Data.

results in significant lifespan extension at specific temperatures, but masculinization of the germline results in drastic lifespan shortening under all tested conditions (Fig. 1 and Supplementary Fig. 1). We further conducted detailed whole-worm lipidomic, intestinal-specific transcriptomic, and genetic interaction analyses using three representative strains, the germline-less *glp-1(e2144)*, the feminized *fem-3(e1996)* and the masculinized *mog-3(q74)*. We demonstrated that although the three different sterile mutants share many similarities, they also exhibit some significant differences. Our findings represent significant resources and pave the way for further investigation to yield insights into how gametogenesis reshapes fat metabolism and impacts organismal longevity.

Our lipid profiling revealed that all three sterile mutants accumulate higher levels of TAGs (~twofold higher than WT). However, the relative proportions of TAGs to PLs remain similar in *fem-3(-)*, *mog-3(-)*, and WT, whereas the proportion of PLs is somewhat lower in *glp-1(-)* (Fig. 2b), which might reflect that *glp-1(-)* mutants having very few germ cells, whereas both *fem-3(-)* and *mog-3(-)* harbor mitotic, meiotic, and their respective differentiated germ cells. These cellular differences among the mutants would inevitably result in differences in lipid profiles, especially the lipids that are membrane constituents of germ cells.

We focused our transcriptomic profiling on the intestine, the major metabolic tissue of *C. elegans*, for both technical reasons, to circumvent the caveat of comparing different sterile strains with varying cellular constituents, and biological reasons, as the germline is known to communicate closely with the intestine to modulate metabolism and longevity. The most prominent changes revealed by the RNA-seq analysis include fat metabolism and stress response genes, consistent with previous transcriptomic analyses focusing on the *glp-1(-)* mutant[16]. Interestingly, especially among upregulated genes, the changes detected in *fem-3(-)* represented a subset of those detected in *glp-1(-)* (Fig. 3b), which correlates with the milder lifespan increase in the *fem-3(-)* compared to the *glp-1(-)* mutant.

Despite the significant overlap in lipid profiles and gene expression changes among the three self-sterile mutants, and the shared phenotype of resistance to *Pseudomonas aeruginosa (PA14)* infection, the three mutants exhibited dramatically different lifespans under

normal culturing conditions. We are therefore particularly intrigued by some of the differences between the long-lived *glp-1(-)* and *fem-3(-)* vs. the short-lived *mog-3(-)* mutants. For example, the *glp-1(-)* and *fem-3(-)* mutants uniquely show altered expression of cuticle/collagen genes. While collagen genes are generally thought to maintain the cuticle integrity, specific collagen genes have been demonstrated to have a major effect on longevity[16,60]. Therefore, it is likely that altered expressions of the many collagen genes in the *glp-1(-)* and *fem-3(-)* mutants contribute to the longevity extension associated with these mutants. On the other hand, *mog-3(-)* worms exhibit unique upregulation of transmembrane transport/solute carrier genes. Similar genes in mammals, including humans, are crucial for male fertility[61], as they enable the transport of ions and small molecules critical for sperm development and function, thereby playing a key role in male reproductive health. Furthermore, the group of "unassigned" genes that show significant expression change in *mog-3(-)* mutants (Fig. 3f) are annotated as "male-associated" based on WormBase Enrichment analysis tool[62,63]. Interestingly, these gene expression changes are detected in intestinal samples, suggesting a potential soma-germline communication.

Integrated analysis of our lipidomic and transcriptomic data highlights a coordinated alteration of the sphingolipid metabolism pathway. Although all three sterile worms showed significant changes in the sphingolipid network, the exact genes and lipid molecules and their degree of change were somewhat different among the mutants. Based on sphingolipid biochemical pathways, sphingosine (So) and ceramide (Cer) can interconvert, and ceramide is further modified to become sphingomyelin (SM) or glucosylceramide (CerG1). It is interesting to note that while all three sterile mutants accumulated significantly higher levels of both SM and CerG1 compared to wild-type, the levels of So were significantly different among the mutants, with the long-lived *glp-1(-)* and *fem-3(-)* mutants storing significantly lower levels, whereas the short-lived *mog-3(-)* mutants stored significantly higher levels (Fig. 2e). This could suggest a regulatory bottleneck at the level of Sphingosine conversion or degradation in these mutants. As noted in the clustering analyses (Supplementary Fig. 5g, h), *glp-1(-)* and *fem-3(-)* mutants share a more similar expression change pattern among the sphingolipid metabolism genes compared to *mog-3(-)*

mutants. This finding hints at selective enzymatic regulation that could preferentially impact Sphingosine levels. However, it remains to be noted that our lipidomic analysis only detected a subset of the different lipid molecules in the pathway, so it remains possible that as the sensitivity of the lipidomic analysis improves, a clearer picture will emerge.

Recently, very long-chain fatty acids glucosylceramides (C22 GlcCer) have been shown to be elevated in *glp-1(-)* mutants and are crucial for maintaining lysosomal function and promoting longevity[64], further bolstering a role of sphingolipid metabolism in lifespan regulation. Future investigation of whether specific alterations in the sphingolipid pathway could confer the differential lifespans of the sterile mutants will likely yield valuable insights.

Since DAF-16 and SKN-1 are two of the best-characterized transcription factors that play a key role in longevity, stress response, and fat metabolism in *C. elegans*[6,16,49,65], we examined their activities in the sterile mutants in greater detail. Our study revealed that SKN-1 is induced by the accumulated fat in all three sterile mutants, irrespective of the lifespan phenotype, consistent with the known role of SKN-1 in responding to lipid toxicity[16]. Therefore, SKN-1 activation promotes the lifespan of the sterile mutants, but it is not likely to contribute to the differential lifespans of these mutants. We revealed that DAF-16 activation is an important factor that mediates the extended lifespan of the *glp-1(-)* and *fem-3(-)* mutants, and its forced activation can reverse the shortened lifespan of the *mog-3(-)* mutant. We additionally demonstrated that DAF-16 activation in *glp-1(-)* and *fem-3(-)* partially depends on the accumulated fat; however, since DAF-16 is not activated in *mog-3(-)* mutant despite its excess lipid accumulation, other factors must contribute to the regulation of DAF-16 activation. It remains possible that the complete absence of sperm differentiation in the *glp-1(-)* and *fem-3(-)* mutants induces a signal to activate DAF-16 in the intestine, a hypothesis that requires further testing. Interestingly, although DAF-16 is similarly activated in both *glp-1(-)* and *fem-3(-)* mutants, *glp-1(-)* shows a greater lifespan extension compared to *fem-3(-)*, again indicating that whereas DAF-16 is important, other factors are also likely to be key in modulating longevity in response to sterility[6,14–16,66].

Detailed transcriptomic and metabolomic comparisons led to the unexpected discovery that masculinized mutants (*mog-3(-), fem-3(-) gain-of-function*) partially mimic MID[21,56]. Recent studies have indicated that during mating, males introduce multiple components into hermaphrodites, including sperm, seminal fluid and its associated biomolecules, as well as pheromones, all appear to contribute to substantial physiological changes and MID in the mated hermaphrodites[21,57,58,67]. We speculate that the resemblance between MOG mutants and mated hermaphrodites stems from two unique combinations in the MOG mutants: (i) Their masculinized germline produces a large number of sperm, high levels of male-specific metabolites[56], and likely other male-derived seminal fluid components. (ii) The excess sperm and male metabolites interact with the soma, which is believed to be hermaphroditic[55,56], creating a situation similar to that of mated hermaphrodites. It is, however, important to note that mog mutants also show key differences from mated hermaphrodites. In particular, mated hermaphrodites greatly increase their reproductive output, which is accompanied by pronounced fat loss[58]; in contrast, *mog* mutants are sterile and retain their fat (Fig. 1 and Supplementary Fig. 1).

At the molecular level, mating has been demonstrated to drive DAF-16 out of the nucleus, thus inactivating this critical pro-longevity transcription factor in several long-lived mutants, including *glp-1(-)*[58]. Thus, eliminating DAF-16 nuclear localization appears to be part of the mechanism / consequence of MID. Interestingly, we observed no DAF-16 nuclear localization and activation in the *mog-3(-)* mutants (Fig. 4), supporting the similarities between *mog* and MID.

We believe MID in mated hermaphrodites and in mated feminized mutants must be a result of metabolic reprogramming, at least partially, that aims to maximize reproductive success. It is known that male-derived seminal fluid contains bioactive molecules that affect lipid metabolism in the hermaphrodites[21,59,68]. In *Drosophila*, lipids like triglycerides are transferred to females during mating and rapidly disperse within the female reproductive tract, modulating female lipid metabolism post-mating[69]. In this regard, it was particularly interesting that we found the Δ9 fatty acid desaturase FAT-7 to be induced both in *mog-3(-)* mutant and in mated hermaphrodites[21]. Interestingly, *fat-6(-); fat-7(-)* double mutant has previously been demonstrated to succumb to MID just like WT[59]. This suggests that mating or *mog* induces *fat-7*, but not *fat-6*, expression, and loss of *fat-7* alone enables partial resistance to MID. However, complete loss of Δ9 desaturase activity in *fat-6(-); fat-7(-)* double mutant, which is known to greatly compromise the health of worms[70], renders them sensitive to MID. How the two closely related Δ9 fatty acid desaturases can have distinct responses upon mating and in *mog* mutants is an interesting question that warrants further investigation.

Additionally, we found that *mog* mutants exhibit overexpression of *che-13* and loss of *che-13* nearly completely rescues the shortened lifespan of *mog* mutants. CHE-13 is essential for sensory cilia development[71,72] and its loss has been demonstrated to compromise the sensory processing of male pheromones and result in resistance to MID[57]. Therefore, our results with *che-13* suggest that *mog* mutants not only produce male-like bioactive compounds but also upregulate the pathway that senses these signals, triggering self-imposed physiological changes and premature lifespan reduction, similar to MID. Taken together, we propose that the *mog* mutants, despite not actively producing progeny, provide a simplified genetic model for studying some aspects of MID, enabling controlled investigation into the physiological trade-offs underlying this phenomenon.

Overall, our study highlights the utility of using different gametogenesis mutants to probe the complex connection between reproduction, metabolism, and longevity. We uncover known pathways, such as DAF-16 in mediating the extended lifespan of the *glp-1(-)* and *fem-3(-)* mutants, and also reveal additional insights, including a possible central role of sphingolipid metabolism in the longevity of self-sterile mutants and that masculinized mutants may serve as a useful genetic model for further investigation of mating-induced metabolic reprogramming and premature death (Fig. 9). Additionally, the drastic effects of feminization and masculinization of the germline have on lifespan underscore the importance of considering sexual differentiation as a significant factor in longevity modulation. Future studies aimed at dissecting the molecular underpinnings of these relationships will enrich our understanding of aging mechanisms and potentially identify targets for interventions aimed at healthy aging in both sexes.

Methods

C. elegans culture methods and strains

C. elegans were maintained using standard protocols. Unless otherwise stated, all strains were grown on nematode growth medium (NGM) plates seeded with *E. coli* OP50-1 as a food source, at the temperatures specified in the text. The following strains were obtained from the Caenorhabditis Genetics Center (CGC): N2, CF1903 *glp-1(e2144)*, MT8186 *mpk-1(oz140)*, JK1466 *gld-1(q485)*, VC2182 *spe-17(ok2593)*, UP749 *ksr-2(dx27)*, VC3391 *RO6F6.8(ok1318)*, TJ356 [*zIs356 (daf-16p::daf-16a/b::gfp + rol-6)*], CL2166 [*dvIs19 (pAF15 gst-4p::GFP::NLS)*], DMS303 [*nIs590 [fat-7p::fat-7::gfp + lin15(+)] V*] and CB3323 [*che-13(e1805)*]. We also generated the following lines by combining strains obtained from the CGC: IU613 [*fem-3(e1996)/nT1 [qIs51] (IV;V)*], IU619 [*fog-3(q470)/hT2 (bli-4(e937) let-?(q782) qIs48) (I;III)*], IU653 [*mog-3(q74)/hT2 (bli-4(e937) let-?(q782) qIs48) (I;III)*], IU658 [*mog-3(q74)/hT2 (bli-4(e937) let-?(q782) qIs48) (I;III); daf-16(mgDf50)/hT2 (bli-4(e937) let-?(q782) qIs48) (I;III)*],
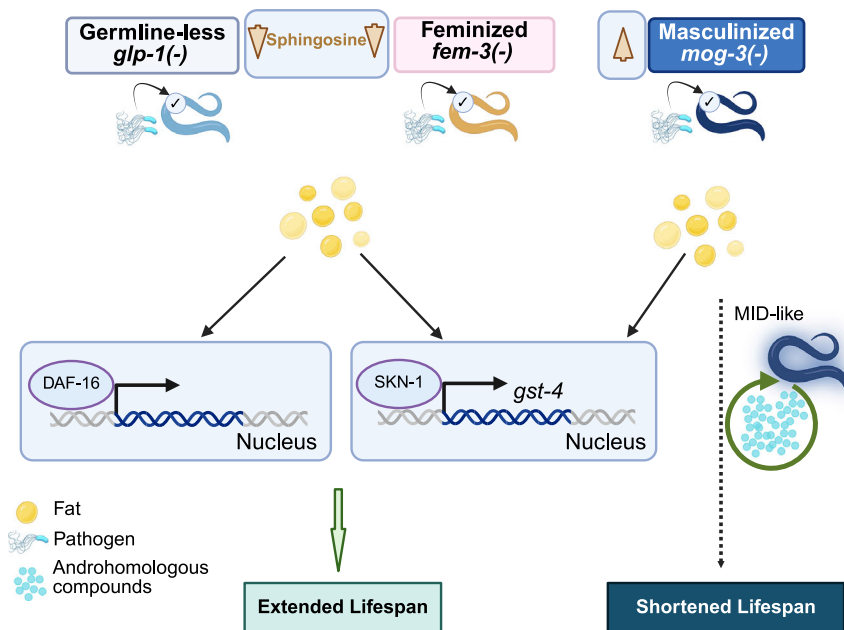
Fig. 9 | Model of lifespan and metabolic differences in sterile germline mutants. Feminized *fem-3(e1996)* mutants are long-lived, though not as long as the well-characterized germline-less *glp-1(e2144)* mutants, while masculinized *mog-3(q74)* mutants are short-lived. All three sterile mutants—*glp-1(e2144)*, *fem-3(e1996)*, and *mog-3(q74)*—accumulate excess neutral lipids, activate SKN-1, show transcriptional upregulation of stress response genes, and display enhanced resistance to Pseudomonas aeruginosa (PA14) infection. Integrated lipidomic and transcriptomic analyses reveal distinct sphingolipid metabolic signatures across these genotypes. Notably, sphingosine levels are lower in the long-lived *glp-1(e2144)* and *fem-3(e1996)* mutants but elevated in the short-lived *mog-3(q74)* mutant. Interestingly, DAF-16 is activated only in the long-lived *glp-1(e2144)* and *fem-3(e1996)* mutants, which likely contributes to their extended longevity. While the sphingosine level differences correlate with lifespan outcomes, it should not be implied that sphingolipid changes act upstream of SKN-1 or DAF-16. *mog-3(q74)* mutants closely resemble mated hermaphrodites and exhibit features of male/mating-induced demise (MID), which likely accounts for their shortened lifespan. (Created in BioRender. Lee, S. (2025) https://BioRender.com/z7nn034).

IU671 [*fem-3(e1996) zIs356 (daf-16p::daf-16a/b::gfp + rol-6)]/nT1 (qIs51) (IV;V)*], IU672 [*glp-1(e2144); zIs356 (daf-16p::daf-16a/b::gfp + rol-6)*], and IU679 [*muIs84 (pAD76 sod-3p::GFP + rol-6(su1006))*], IU827 [*fat-7(wa36) I*], IU740 [*mog-3(q74)/hT2 [bli-4(e937) let-?(q782) qIs48] (I;III); fat-7(wa36) V*], IU773 [*mog-3(q74)/hT2 [bli-4(e937) let-?(q782) qIs48] (I;III); nIs590 [fat-7::fat-7::GFP + lin15(+)] V*] and IU830 [IU653 [*mog-3(q74)/hT2 [bli-4(e937) let-?(q782) qIs48] (I;III)]; che-13(e1805) I*].

Oil red O (ORO) staining

The ORO staining procedure was carried out as previously described with slight modifications[73]. A 0.5 g ORO stock solution was prepared by dissolving the ORO (Sigma-Aldrich, O0625) in 100 ml of 100% isopropanol and left to equilibrate for 2 days on a magnetic stirrer. -100 worms were collected in 500 μl PBST (PBS + 0.1% Tween-20), washed once with PBS, and fixed in 4% formaldehyde fixative (800 μl water, 100 μl 10× PBS, and 100 μl formaldehyde) for 30 min. After removal of the fixative, the worms were washed with PBST and PBS once each, and then treated with 60% isopropanol for 2 min. 200 μl working solution of ORO (60% ORO stock + 40% water) was added to each tube and incubated for 2–3 h. The worms were washed twice with PBS, and 10 μl of Vectashield mounting medium was added to each tube. For imaging, the worms were mounted on a 2% agarose pad and images were captured using a Leica compound microscope (Leica DM5000B).

ORO extraction and calorimetric estimation

All steps of the ORO staining protocol were carefully followed up until the first wash with PBS after the ORO staining step. The worms were washed once with 500 μl of PBS and twice with distilled water for 5 min each. Subsequently, they were incubated twice in 60% isopropanol for 5 min each. To extract the bound ORO, the worms were placed in 100 μl of 100% isopropanol and incubated for 5–7 min on a rocking platform. 85–90 μl of the supernatant was then transferred to a 96-well plate, and the absorbance was measured at 492 nm. A 100% isopropanol control was used to subtract the background signal.

RNAi treatment

The RNAi procedure was carried out as previously described, with slight modifications[74]. The RNAi was conducted by feeding the worms with HT115 bacteria that expressed double-stranded RNA of the target gene. The RNAi clones were obtained from RNAi feeding libraries created by Julie Ahringer and Marc Vidal's laboratories[75,76]. To begin, a single colony of RNAi bacteria was streaked onto an LB agar plate containing ampicillin (100 μg/ml) and grown overnight at 37 °C. The following day, a single bacterial colony was inoculated into 5 mL of LB broth containing ampicillin (100 μg/ml) and tetracycline (15 μg/ml) and incubated overnight in a shaker at 37 °C. To verify the accuracy of the RNAi clone, the plasmid was extracted and submitted for sequencing. Upon confirmation of the correct RNAi plasmid insert, a single colony of the bacteria was cultured overnight in 5 mL of LB broth containing ampicillin (100 μg/ml) and tetracycline (12.5 μg/ml) at 37 °C in a shaker. For every RNAi experiment, a control culture of bacteria containing the L4440 plasmid was also included.

The overnight culture (5% of the final culture) was then inoculated in the desired volume of LB broth containing ampicillin (100 μg/ml) and incubated for an additional 3–4 h at 37 °C in a shaker. Once the optical density (OD600) reached approximately 0.6, the culture was induced with 1 mM IPTG (Isopropyl β-D-1-thiogalactopyranoside) and incubated for an additional 2–3 h at 37 °C in a shaker. The culture was then centrifuged at 3000 × g for 15 min at room temperature, and the bacterial pellet was resuspended in the desired volume of the same supernatant (200 μl per plate). Two or three RNAi plates were prepared for each target gene in each experiment, each containing 200 μl of bacterial culture spread on NGM agar plate (no streptomycin) containing ampicillin (100 μg/ml), tetracycline (15 μg/ml), and IPTG

(1 mM). The plates were dried under a hood, and 10–15 adult worms were allowed to lay eggs overnight on each plate. The worms from the first set of RNAi plates were transferred to a new set of RNAi plates, and the embryos were collected for 2–3 h. The embryos laid on the second set of RNAi plates were grown to the desired stage, and then the relevant phenotypes were scored.

Lifespan analysis

Lifespan assays were performed with some modifications as described earlier[74]. 10–15 gravid worms were placed on plates containing the desired bacterial food, and approximately 200 embryos were collected. Upon reaching the 1-day adult stage, 30 worms were transferred to each of three RNAi plates and their status was monitored daily or every other day by counting the number of live or dead worms. Death was confirmed by the absence of movement after gentle touching of the worm's nose. Cases of death by rupturing, bursting, or runoff were considered censored. For lifespan assays on FUDR plates, NGM plates were supplemented with 50 μM 5-fluorodeoxyuridine (FUDR) and seeded with *E. coli* OP50. For male/mating-induced demise (MID) lifespan analysis, approximately 30 hermaphrodites were placed on a feeding plate with an equal number of wild-type males and allowed to mate for 48 h before the males were removed. Three plates were prepared per genotype for each replicate. The lifespan data were analyzed using the OASIS online survival analysis tool[77] available at https://sbi.postech.ac.kr/oasis2/.

TAG (Triacyglycerides) estimation by colorimetry

Approximately 100 worms were collected in PBST, washed three times, and then suspended in 100 μL of cold PBST. The mixture was flash-frozen in liquid nitrogen and thawed on ice. The worms were homogenized using a motorized pestle (Kontes: 749540-0000) and centrifuged for 3 min at 13,000 × *g* at 4 °C. A portion (10–20 μl) of the supernatant was set aside for protein measurement. The remaining supernatant was heated at 70 °C for 10 min. 10–25 μl of the heated sample (in two replicates) and 200 μl of Infinity Triglyceride Reagent (ThermoFisher, TR22421) were added to separate wells of a 96-well plate and incubated at 37 °C for 30 min. The plate was wrapped in aluminum foil for the duration of the experiment, and absorbance was measured at 540 nm.

Pseudomonas aeruginosa (PA14) slow-killing and survival assay

The PA14 slow-killing assay was modified from the method described earlier[41]. A single colony of PA14 was inoculated into LB media and cultured overnight at 37 °C in a shaker. The following day, the culture was concentrated 20-fold and spread on PA14 slow-killing plates, then dried under a hood. Approximately 10–15 gravid worms were placed on the PA14 plate, and around 200 embryos were collected. When the worms reached the L4 stage, 50 μM FUDR (5-fluoro-2′-deoxyuridine) was added to both the control and experimental PA14 plates to inhibit reproduction. The following day, 30 worms were transferred to each of three PA14 plates and the number of live or dead worms were scored every 12 h until all worms had died. Death by rupture, bursting, or crawling off the plates was considered censored. The data were analyzed using the OASIS online survival analysis tool[77].

RNA isolation and library preparation for RNA-seq

RNA isolation was performed as previously described with some modifications[74]. For the collection of whole-worm samples, approximately 200 worms were collected in TRI reagent (MRC, Cat No. TR 118). For the collection of intestinal tissue, 100–120 worms were dissected using a syringe needle, and 70–80 intestines were collected in TRI reagent. Three biological replicates were collected for each genotype. The samples were homogenized in 10 volumes of TRI reagent (500 μl) by performing several rounds of freeze-thaw cycles in liquid nitrogen. Subsequently, 200 μl of chloroform was added per 1 ml of TRI reagent

(MRC, TR118), the tube was vortexed for 15 s, and the mixture was incubated at room temperature for 2–3 min. The samples were then centrifuged at 12,000 × *g* for 15 min at 4 °C in a refrigerated centrifuge. The upper colorless layer was collected in a 1.5 ml microcentrifuge tube and 0.5 mL of isopropanol per mL of TRIZOL was added. The tube was mixed well and the sample was incubated at room temperature for 10 min. The tube was then centrifuged at 12,000 × *g* for 10 min at 4 °C. The supernatant was removed, and the transparent RNA pellet was washed with 1 ml of 75% ethanol. After removing all residual ethanol, the pellet was air-dried for 5–7 min at room temperature and the RNA was dissolved in RNase-free water. The RNA was then purified using the RNeasy Mini Kit (Qiagen, 74106) (for whole worm samples) and Zymo RNA Clean-up kit (Zymo Research, Cat. No. R1014) (for intestinal samples). A library for RNA-seq was prepared using the Ovation Human FFPE RNA-Seq Library Systems (NuGEN) (for whole worm samples) and the QuantSeq 3′ mRNA-Seq Library Prep Kit for Illumina (FWD) (Lexogen) (for intestinal samples).

RNA-seq data analysis

To obtain the total read counts of RNA-seq data using Linux, the following method was employed: The FASTQ files were downloaded by saving and running a download script (download.sh). Quality control of the downloaded FASTQ files was performed using FastQC, with the analysis run in parallel. The read length of the FASTQ files was checked by extracting and measuring the length of the sequences. The STAR software was used to build the genome index, utilizing the genome FASTA file and the corresponding GTF file. The alignment of reads was performed using STAR, executed in parallel with a predefined list of commands. This alignment process included generating BAM files sorted by coordinate and counting gene-specific reads. Unique mapped reads were counted using SAMtools by filtering the aligned reads in the BAM files. The total read counts were verified using the log output files generated by STAR. The BAM files were indexed using SAMtools in parallel. The read count matrix was generated by STAR and counts for reads aligned with the plus and minus strands of RNA. For 3′ RNA-seq, the counts from the plus strand column were used.

To generate a differentially expressed gene list and perform PCA plot analysis from total read count data, the following methods were employed: first, the necessary R libraries were loaded, including DESeq2, ggplot2, dplyr, apeglm, and ggfortify. The total read count data was read into a matrix format, and the corresponding metadata was read into a data frame. A DESeq DataSet object was created from the count matrix and metadata. Size factors for normalization were estimated and applied to the count data, and the normalized counts were then saved to a file. Genes with low counts were filtered out to retain those with at least three counts greater than or equal to five in any of the experimental groups. The dataset was then reduced to include only the genes that passed this filter. Differential expression analysis was conducted using the DESeq function, and the results were extracted. The results of the differential expression analysis were ordered by adjusted *p*-value or False Discovery Rate (FDR). Finally, a PCA plot was generated using the ggplot2 package to visualize the variance explained by the principal components. Principal component analysis (PCA) was performed using R[30].

Venn diagram generation

Venn diagrams were generated using the online tool DeepVenn[78] online tool, with additional formatting performed in Microsoft Excel.

Motif analysis

First, the necessary R packages were installed and loaded, including biomaRt and Biostrings. The differentially expressed gene list was loaded, and a connection to the Ensembl BioMart database was established using the biomaRt package, specifying the use of the "*C. elegans* gene Ensembl" dataset. Promoter sequences, defined as the

2 kb upstream region from the transcription start site (TSS) of each gene in the gene list, were retrieved from this database. Similarly, a background promoter list for each genotype was obtained to serve as background sequences. For the background sequence, promoters were derived from genes that were not differentially expressed in these genotypes. The retrieved promoter sequences were then converted into FASTA format using the Biostrings package.

Finally, the promoter sequences were saved for further motif analysis using "The MEME Suite"[79]. The promoters of differentially expressed genes were used as input in the MEME suite, while promoters of unchanged genes were used as background sequences. Simple Enrichment Analysis (SEA) was then performed to identify enriched motifs in each genotype[80].

Sample preparation for LC-MS-based Lipidomic analysis

Samples were extracted following the protocol described by Witting et al. (2015)[81] with some modifications. 20–25 gravid worms were placed on ten 6-cm NGM plates that were seeded with OP50 bacterial food. Embryos were then collected and when they reached the 1-day adult stage, 1500 to 2000 worms were picked and placed on a seeded plate. The worms were then washed off the plate using M9 buffer + 0.01% Tween-20 in a 5 ml tube. They were further washed once with M9 buffer and double-distilled water. The worms were quenched with 500 μl of cold (−20 °C) MeOH and the sample was flash-frozen in liquid nitrogen and stored at −80 °C before further processing. The sample was then thawed on ice, 1.7 ml of Methyl tert-butyl ether (MTBE) was added, and the sample was vigorously vortexed. The sample was then handed over to the Cornell Metabolomics facility for further processing and Liquid Chromatography-Mass Spectrometry (LC-MS) analysis. At the facility, 120 μL of water was added to the samples, which were then sonicated for an additional 15 min. Phase separation was achieved by centrifugation at $14,000 \times g$ for 15 min at 4 °C. The upper organic phase was transferred to a 4 mL glass vial, while the remaining lower phase underwent a second extraction with an additional 160 μL MTBE for 15 min. After a second round of centrifugation, the organic layers were pooled and evaporated using a SpeedVac vacuum concentrator (Thermo Scientific, Dreieich, Germany). The final residue was reconstituted in 150 μL of ACN/iPrOH/water (65/30/5, v/v/v) for subsequent analysis. The internal standard (IS) mixture spiked into each sample prior to analysis and used for normalization consisted of 25 μg/mL of TG (15:0)3, PC (17:0)2, PG (14:0)2, lysoPC (20:0), and FA (18:1), Cer (18:01/17) and Cholesteryl ester (17:0). UHPLC-MS lipidomics analysis was performed using a Thermo Vanquish UHPLC System with an Accucore C30 column (2.6 μm, 2.1 mm ID × 150 mm) at a flow rate of 260 μL/min. The column temperature was maintained at 55 °C, while the autosampler tray was set at 4 °C. A 2 μL injection volume was used. Mobile phases consisted of Solvent A (60% ACN, 40% H_2O, 10 mM Ammonium Formate with 0.1% Formic Acid) and Solvent B (90% IPA, 10% ACN, 10 mM Ammonium Formate with 0.1% Formic Acid). MS experimental conditions included an ESI voltage of 3 kV, sheath gas flow rate of 50 (arbitrary units), aux gas flow rate of 5, sweep gas flow rate of 1, capillary temperature of 320 °C, S-Lens RF level of 50, and aux gas heater temperature of 350 °C, with both positive and negative mode acquisition. Data Analysis was conducted using LipidSearch software and SIMCA (Umetrics, Umeå, Sweden). Non-targeted lipidomics data processing included searching individual data files for product ion MS/MS spectra of lipid precursor ions with MS/MS fragment ions predicted for all precursor ions measured within ±5 ppm. A match score was assigned to the best-matching candidate, and search results from positive and negative ion files were aligned within a retention time window of ±0.1 min before merging annotated lipids. False positives were minimized using predefined filtering criteria, and data were normalized using internal standards specific to different lipid classes. Data normalization was carried out using internal standards specific to each lipid class. Ceramide(18:1/17) was used for

ceramides and sphingomyelin; CholesterylEster(17:0) for cholesteryl esters; LysoPC(20:0/0:0) for lysophosphatidylcholine (LPC); PC(17:0)2 for phosphatidylcholine (PC); PG(14:0)2 for phosphatidylglycerol (PG) and cardiolipin (CL); PS(16:0)2 for phosphatidylserine (PS), phosphatidylinositol (PI), and phosphatidylethanolamine (PE); and TG(15:0)3 for monoacylglycerols (MG), diglycerol (DG), and triglycerides (TG).

Free fatty acid extraction and analysis

Samples were extracted following the same protocol as used for Lipidomics. For normalization, an internal standard (IS) mixture was included in the reconstitution solvent at a concentration of 25 μg/ml of heptadecanoic acid. Lipid analysis was performed using an Ultra-High-Performance Liquid Chromatography (UHPLC) system (Thermo Vanquish UHPLC System) equipped with an Accucore C30 column (2.6 μm, 2.1 mm id × 150 mm). The flow rate was set to 260 μL/min, with a column temperature of 30 °C and an autosampler tray temperature of 4 °C. The injection volume was 2 μL, and the mobile phase solvents were (A) 10 mM Ammonium Acetate in Isopropanol:Acetonitrile (9:1) and (B) 10 mM Ammonium Acetate in Water:Acetonitrile (6:4). For mass spectrometry (MS) analysis, data were acquired in negative mode with an electrospray ionization (ESI) voltage of 3 kV. Additional MS parameters included a sheath gas flow rate of 50 (arbitrary units), an auxiliary gas flow rate of 5, a sweep gas flow rate of 1, a capillary temperature of 320 °C, an S-lens RF level of 50, and an auxiliary gas heater temperature of 350 °C. Lipid identification and quantification were performed using Thermo Scientific Lipid-Search software (version 4.1) and SIMCA (Umetrics, Umeå, Sweden). Data were normalized using heptadecanoic acid to ensure consistency across samples.

Lipidomic data analysis

Differential expression of each lipid molecule "features" was analyzed using EdgeR under R studio. A 5% false discovery rate (FDR) was used to determine significant differential changes. Principal component analysis (PCA) was performed using R[30].

Lipidomic data set enrichment analysis

For lipid enrichment analysis a Fisher's Exact Test was performed for each lipid class, calculating Odds Ratios (OR) or enrichment scores and p-values, with the total detected lipidome (1224 lipids) serving as the reference. A contingency table was constructed for each lipid class, and Fisher's Exact Test was applied. To visualize the enrichment scores and p-values of lipid classes across conditions, we used ggplot2 to create a bubble plot, where the circle size represents the enrichment score, and the color represents the p-value. The dataset was first transformed into a long format using melt() from the reshape2 package to facilitate plotting. The bubble plot was generated using ggplot() with geom_point(), where the size aesthetic mapped to enrichment scores and the color aesthetic mapped to p-values.

Gene set enrichment analysis

Gene set enrichment analysis was performed using the WormCat[38]. In our differential analysis, we found a number of germline-specific genes to be significantly changed, specifically downregulated in the sterile mutants (Supplementary Data 3, blue-colored cells denote the germline-enriched genes). We concluded that during the process of intestinal dissection, some amount of gonad must had inadvertently been associated, due to the closely linked anatomy of these two tissues. Therefore, we filtered out germline-enriched genes based on Reinke et al. (2004) and conducted the Gene Set Enrichment Analysis after removing these germline genes.

STRING analysis

STRING analysis was performed using an online tool, STRING, which is designed for Protein-Protein Interaction and Functional Enrichment

Analysis[39]. A list of differentially regulated genes was uploaded to the platform and was clustered using k-means clustering based on their Gene Ontology terms. For this analysis, we specifically used differentially expressed genes related to fat metabolism and stress response, as annotated by WormCat[38].

Omics data integration

The integration of transcriptomic and lipidomic data was performed using MetaboAnalyst[40]. This module was introduced in MetaboAnalyst 3.0. In this module, the lists of differentially expressed genes and differentially changed lipids were uploaded with their log2 fold change. The integration between these datasets was assessed, and genes and lipids were mapped to relevant KEGG metabolic pathways for over-representation analysis, with significance determined by the False Discovery Rate (FDR).

Whole worms DAPI staining

50–100 worms were collected into a 1.5 mL microcentrifuge tube and washed twice with 1 mL PBST (PBS + 0.1% Tween-20) for 2–3 min per wash. After washing, PBST was removed, and the worms were fixed in 100% methanol for 2 min at room temperature. The methanol was then removed, and the worms were stained with a DAPI staining solution (1 µL of 2 µg/mL DAPI in 100 µL of 100% methanol) for 30 min at room temperature. Following staining, the worms were washed three times with 1 mL PBST for 5 min per wash. After the final wash, 8 µL of Vectashield was added, and the worms were mounted on a 2% agarose pad for microscopy. Images were acquired using a Leica compound microscope (Leica DM5000B).

EdU (5-ethynyl-2'-deoxyuridine) Staining

EdU staining was performed as previously described, with modifications[82], using the Click-iT® EdU Imaging Kit (ThermoFisher Cat. No. C10337). For EdU incorporation, 50 worms were washed and collected from plates using M9 buffer containing 0.1% Triton ×-100 (M9_Triton) and subsequently washed twice with 1 ml M9_Triton. 50 µl of M9_Triton containing the worms were transferred into a fresh 1.5 ml microcentrifuge tube, followed by the addition of 50 µl of 10 mM EdU. The worms were gently mixed and incubated on a shaker for 40 min at 22–25 °C. After incubation, the worms were washed twice with 1 ml M9_Triton. Next, 30 µl of EBT (110 µl 10× egg buffer, 10 µl 10% Tween-20, 6.5 µl 10% tetramisole, and 850 µl distilled water to a total of 976.5 µl) was pipetted onto a coverslip, and approximately 50 worms were transferred into the EBT drop. The worms were anesthetized for 20 s before their heads were cut to extrude the gonads. The gonads were collected into a 1.5 ml microcentrifuge tube, fixed with 4% formaldehyde prepared in egg buffer for 20 min, and washed twice with 1 ml of 3% BSA in PBS. For permeabilization, the gonads were incubated in 1 ml of 1% Triton ×-100 in PBS at room temperature for 20 min. After permeabilization, the buffer was removed, and the samples were washed twice with 1 ml of 3% BSA in PBS. Subsequently, 0.5 ml of the Click-iT® reaction cocktail (prepared as per the kit instructions) was added, and the tubes were incubated at room temperature for 30 min on a shaker, protected from light. Following incubation, the reaction cocktail was removed, and the samples were washed twice with 1 ml of 3% BSA in PBS. For the chase reaction, worms were transferred onto seeded NGM plates immediately after the EdU incubation step. After 24 h, worms were collected and washed twice with 1 ml M9-Triton, and the dissection process was then resumed. Finally, 8 µl of Vectashield was added, and the worms were mounted on a 2% agarose pad for imaging. Images were acquired using a Keyence BZ-X810 microscope.

Mating setup

Approximately 15 gravid adult hermaphrodites were placed on 6-cm feeding plates seeded with the desired bacteria, and embryos were collected over a 2-h period before the mothers were removed. Once the embryos reached the L4 stage, 50 hermaphrodites were transferred to a feeding plate with an equal number of wild-type males. After 48 h of mating, worms were collected for either lifespan assays or imaging analysis.

Reporting summary

Further information on research design is available in the Nature Portfolio Reporting Summary linked to this article.

Data availability

RNA-sequencing data are available on NCBI under the project ID PRJNA1175675. Source Data underlying the figures are provided with this paper. Raw lipidomic data, along with annotation details, are provided in Supplementary Data 1. Source data are provided with this paper.

References

1. Kirkwood, T. B. L. & Rose, M. R. *Evolution of Senescence: Late Survival Sacrificed for Reproduction*. https://royalsocietypublishing.org/ (1991).
2. Arantes-Oliveira, N., Apfeld, J., Dillin, A. & Kenyon, C. Regulation of life-span by germ-line stem cells in *Caenorhabditis elegans*. *Science* **295**, 502–505 (2002).
3. Drori, D. & Folman, Y. Environmental effects on longevity in the male rat: exercise, mating, castration and restricted feeding. *Exp. Gerontol.* **11**, 25–32 (1976).
4. Flatt, T. et al. *Drosophila* germ-line modulation of insulin signaling and lifespan. https://doi.org/10.1073/pnas.0709128105 (2008).
5. Hamilton, J. B. & Mestler, G. E. Mortality and survival: comparison of eunuchs with intact men and women in a mentally retarded population. *J. Gerontol.* **24**, 395–411 (1969).
6. Hsin, H. & Kenyon, C. Signals from the reproductive system regulate the lifespan of *C. elegans*. *Nature* **399**, 362–366 (1999).
7. Min, K. J., Lee, C. K. & Park, H. N. The lifespan of Korean eunuchs. *Curr. Biol.* **22**, R792-3 (2012).
8. Westendorp, R. G. J. & Kirkwood, T. B. L. Human longevity at the cost of reproductive success. *Nature* **396**, 743–746 (1998).
9. Rodrigues, M. A. et al. Germline proliferation trades off with lipid metabolism in *Drosophila*. https://doi.org/10.1093/evlett/qrad059.
10. Lind, M. I. et al. Sex-specific growth and lifespan effects of germline removal in the dioecious nematode *Caenorhabditis remanei*. *Aging Cell* e14290 https://doi.org/10.1111/ACEL.14290 (2024).
11. Moses, E. et al. The killifish germline regulates longevity and somatic repair in a sex-specific manner. *Nat. Aging* **4**, 791–813 (2024).
12. Wang, M. C., O'Rourke, E. J. & Ruvkun, G. Fat metabolism links germline stem cells and longevity in *C. elegans*. *Science* **322**, 957–960 (2008).
13. Amrit, F. R. G. et al. DAF-16 and TCER-1 facilitate adaptation to germline loss by restoring lipid homeostasis and repressing reproductive physiology in *C. elegans*. *PLoS Genet.* **12**, e1005788 (2016).
14. Goudeau, J. et al. Fatty acid desaturation links germ cell loss to longevity through NHR-80/HNF4 in *C. elegans*. *PLoS Biol.* **9**, e1000599 (2011).
15. Ratnappan, R. et al. Germline signals deploy NHR-49 to modulate fatty-acid β-oxidation and desaturation in somatic tissues of *C. elegans*. *PLoS Genet.* **10**, e1004829 (2014).
16. Steinbaugh, M. J. et al. Lipid-mediated regulation of SKN-1/Nrf in response to germ cell absence. *Elife* **4**, e07836 (2015).
17. Ramachandran, P. V. et al. Lysosomal signaling promotes longevity through adjusting mitochondrial activity graphical abstract. *Dev. Cell* **48**, 685–696 (2019).
18. Hubbard, E. J. A. & Greenstein, D. Introduction to the germ line. *WormBook* 1–4 https://doi.org/10.1895/WORMBOOK.1.18.1 (2005).

19. Kimble, J. & Crittenden, S. L. Germline proliferation and its control. *WormBook* 1–14 https://doi.org/10.1895/WORMBOOK.1.13.1 (2005).

20. Ellis, R. & Schedl, T. Sex determination in the germ line *. https://doi.org/10.1895/wormbook.1.82.2 (2007).

21. Booth, L. N. et al. Males induce premature demise of the opposite sex by multifaceted strategies. *Nat. Aging* **2**, 809–823 (2022).

22. Hanazawa, M. et al. The *Caenorhabditis elegans* eukaryotic initiation factor 5A homologue, IFF-1, is required for germ cell proliferation, gametogenesis and localization of the P-granule component PGL-1. *Mech. Dev.* **121**, 213–224 (2004).

23. Austin, J. & Kimble, J. *glp-1* is required in the germ line for regulation of the decision between mitosis and meiosis in *C. elegans*. *Cell* **51**, 589–599 (1987).

24. Killian, D. J. & Hubbard, E. J. A. *C. elegans pro-1* activity is required for soma/germline interactions that influence proliferation and differentiation in the germ line. *Development* **131**, 1267–1278 (2004).

25. Francis, R., Barton, M. K., Kimble, J. & Schedl, T. *gld-1*, a tumor suppressor gene required for oocyte development in *Caenorhabditis elegans*. *Genetics* **139**, 579–606 (1995).

26. Kasturi, P. et al. The *C. elegans* sex determination protein MOG-3 functions in meiosis and binds to the CSL co-repressor CIR-1. *Dev. Biol.* **344**, 593–602 (2010).

27. Suh, N. et al. FBF and its dual control of *gld-1* expression in the *Caenorhabditis elegans* germline. https://doi.org/10.1534/genetics.108.099440.

28. Folick, A. et al. Lysosomal signaling molecules regulate longevity in *Caenorhabditis elegans*. *Science* **347**, 83–86 (2015).

29. Qi, W. et al. The ω-3 fatty acid α-linolenic acid extends *Caenorhabditis elegans* lifespan via NHR-49/PPARα and oxidation to oxylipins. *Aging Cell* **16**, 1125 (2017).

30. Robinson, M. D., McCarthy, D. J. & Smyth, G. K. edgeR: a Bioconductor package for differential expression analysis of digital gene expression data. *Bioinformatics* **26**, 139–140 (2010).

31. Han, S. et al. Mono-unsaturated fatty acids link H3K4me3 modifiers to *C. elegans* lifespan. *Nature* **544**, 185–190 (2017).

32. Shmookler Reis, R. J. et al. Modulation of lipid biosynthesis contributes to stress resistance and longevity of *C. elegans* mutants. *Aging* **3**, 125 (2011).

33. Wan, Q. L. et al. The effects of age and reproduction on the lipidome of *Caenorhabditis elegans*. Oxid. Med. Cell. Longev. 2019, 5768953 (2019).

34. Lin, K., Hsin, H., Libina, N. & Kenyon, C. Regulation of the *Caenorhabditis elegans* longevity protein DAF-16 by insulin/IGF-1 and germline signaling. *Nat. Genet.* **28**, 139–145 (2001).

35. Berman, J. R. & Kenyon, C. Germ-cell loss extends *C. elegans* life span through regulation of DAF-16 by *kri-1* and lipophilic-hormone signaling. *Cell* **124**, 1055–1068 (2006).

36. Wormatlas Homepage. https://www.wormatlas.org/.

37. Reinke, V., Gil, I. S., Ward, S. & Kazmer, K. Genome-wide germline-enriched and sex-biased expression profiles in *Caenorhabditis elegans*. *Development* **131**, 311–323 (2004).

38. Holdorf, A. D. et al. WormCat: an online tool for annotation and visualization of *Caenorhabditis elegans* genome-scale data. *Genetics* **214**, 279–294 (2020).

39. Szklarczyk, D. et al. STRING v11: protein-protein association networks with increased coverage, supporting functional discovery in genome-wide experimental datasets. *Nucleic Acids Res.* **47**, 607–613 (2018).

40. MetaboAnalyst. https://www.metaboanalyst.ca/.

41. Tan, M., Mahajan-Miklos, S. & Ausubel, F. M. Killing of *Caenorhabditis elegans* by *Pseudomonas* aeruginosa used to model mammalian bacterial pathogenesis. **96**, 715–720 www.pnas.org (1999).

42. Introduction - MEME Suite. https://meme-suite.org/meme/.

43. Kenyon, C., Chang, J., Gensch, E., Rudner, A. & Tabtiang, R. A *C. elegans* mutant that lives twice as long as wild type. *Nature* **366**, 461–464 (1993).

44. Lakowski, B. & Hekimi, S. The genetics of caloric restriction in *Caenorhabditis elegans*. *Proc. Natl. Acad. Sci. USA* **95**, 13091 (1998).

45. Hsu, A. L., Murphy, C. T. & Kenyon, C. Regulation of aging and age-related disease by DAF-16 and heat-shock factor. *Science* **300**, 1142–1145 (2003).

46. Libina, N., Berman, J. R. & Kenyon, C. Tissue-specific activities of *C. elegans* DAF-16 in the regulation of lifespan tissues play an important role in establishing the animal's rate of aging. *Cell* **115**, 489–502 (2003).

47. Yamawaki, T. M., Arantes-Oliveira, N., Berman, J. R., Zhang, P. & Kenyon, C. Distinct activities of the germline and somatic reproductive tissues in the regulation of *Caenorhabditis elegans*' longevity. *Genetics* **178**, 513–526 (2008).

48. Li, S. T. et al. DAF-16 stabilizes the aging transcriptome and is activated in mid-aged *Caenorhabditis elegans* to cope with internal stress. *Aging Cell* **18**, e12896 (2019).

49. Tullet, J. M. A. et al. Direct inhibition of the longevity-promoting factor SKN-1 by insulin-like signaling in *C. elegans*. *Cell* **132**, 1025–1038 (2008).

50. Bishop, N. A. & Guarente, L. Two neurons mediate diet-restriction-induced longevity in *C. elegans*. *Nature* **447**, 545–549 (2007).

51. Link, C. D. & Johnson, C. J. Reporter transgenes for study of oxidant stress in *Caenorhabditis elegans*. *Methods Enzymol.* **353**, 497–505 (2002).

52. Varkey, J. P., Muhlrad, P. J., Minniti, A. N., Do, B. & Ward, S. The *Caenorhabditis elegans* spe-26 gene is necessary to form spermatids and encodes a protein similar to the actin-associated proteins kelch and scruin. *Genes Dev.* **9**, 1074–1086 (1995).

53. Mitchell, D. H., Stiles, J. W., Santelli, J. & Rao Sanadi, D. Synchronous growth and aging of *Caenorhabditis elegans* in the presence of fluorodeoxyuridine. *J. Gerontol.* **34**, 28–36 (1979).

54. Gems, D. & Riddle, D. L. Genetic, behavioral and environmental determinants of male longevity in *Caenorhabditis elegans*. *Genetics* **154**, 1597–1610 (2000).

55. Barton, M. K., Schedl, T. B. & Kimble, J. Gain-of-function mutations of fem-3, a sex-determination gene in *Caenorhabditis elegans*. *Genetics* **115**, 107–119 (1987).

56. Burkhardt, R. N. et al. Sex-specificity of the *C. elegans* metabolome. *Nat. Commun.* **14**, 1–15 (2023).

57. Maures, T. J. et al. Males shorten the life span of *C. elegans* hermaphrodites via secreted compounds. *Science* **343**, 541–544 (2014).

58. Shi, C. & Murphy, C. T. Mating induces shrinking and death in Caenorhabditis mothers. *Science* **343**, 536–540 (2014).

59. Choi, L. S., Shi, C., Ashraf, J., Sohrabi, S. & Murphy, C. T. Oleic acid protects Caenorhabditis mothers from mating-induced death and the cost of reproduction. *Front. Cell Dev. Biol.* **9**, 690373 (2021).

60. Ewald, C. Y., Landis, J. N., Abate, J. P., Murphy, C. T. & Blackwell, T. K. Dauer-independent insulin/IGF-1-signalling implicates collagen remodelling in longevity. *Nature* **519**, 97 (2015).

61. Wang, H., McGoldrick, L. L. & Chung, J. J. Sperm ion channels and transporters in male fertility and infertility. *Nat. Rev. Urol.* **18**, 46–66 (2021).

62. WormBase: Nematode Information Resource. https://wormbase.org/#012-34-5.

63. Angeles-Albores, D., Raymond, R. Y., Chan, J. & Sternberg, P. W. Tissue enrichment analysis for *C. elegans* genomics. *BMC Bioinforma.* **17**, 1–10 (2016).

64. Wang, F. et al. Saturated very long chain fatty acid configures glycosphingolipid for lysosome homeostasis in long-lived *C. elegans*. *Nat. Commun. 2021* **12**, 1–14 (2021).

65. Zečić, A. & Braeckman, B. P. DAF-16/FoxO in *Caenorhabditis elegans* and its role in metabolic remodeling. *Cells* **9**, 109 (2020).

66. Lapierre, L. R., Gelino, S., Meléndez, A. & Hansen, M. Autophagy and lipid metabolism coordinately modulate life span in germline-less *C. elegans*. *Curr. Biol.* **21**, 1507–1514 (2011).

67. Shi, C., Runnels, A. M. & Murphy, C. T. Mating and male pheromone kill Caenorhabditis males through distinct mechanisms. *Elife* **6**, e23493 (2017).

68. Chen, M. & Gong, J. A male seminal fluid protein SFP-1 regulates hermaphrodite post-mating longevity and fat metabolism in Caenorhabditis elegans. Preprint at https://www.biorxiv.org/content/10.1101/2024.09.09.612157v1 (2024).

69. Mark Wainwright, S. et al. *Drosophila* sex peptide controls the assembly of lipid microcarriers in seminal fluid. *Proc. Natl. Acad. Sci USA* **118**, e2019622118 (2021).

70. Brock, T. J., Browse, J. & Watts, J. L. Fatty acid desaturation and the regulation of adiposity in *Caenorhabditis elegans*. *Genetics* **176**, 865–875 (2007).

71. Perkins, L. A., Hedgecock, E. M., Thomson, J. N. & Culotti, J. G. Mutant sensory cilia in the nematode *Caenorhabditis elegans*. *Dev. Biol.* **117**, 456–487 (1986).

72. Haycraft, C. J., Schafer, J. C., Zhang, Q., Taulman, P. D. & Yoder, B. K. Identification of CHE-13, a novel intraflagellar transport protein required for cilia formation. *Exp. Cell Res.* **284**, 249–261 (2003).

73. O'Rourke, E. J., Soukas, A. A., Carr, C. E. & Ruvkun, G. *C. elegans* major fats are stored in vesicles distinct from lysosome-related organelles. *Cell Metab.* **10**, 430–435 (2009).

74. Wang, W. et al. SET-9 and SET-26 are H3K4me3 readers and play critical roles in germline development and longevity. *Elife* **7**, e34970 (2018).

75. Kamath, R. S. et al. Systematic functional analysis of the *Caenorhabditis elegans* genome using RNAi. *Nature* **421**, 231–237 (2003).

76. Rual, J. F. et al. Toward improving *Caenorhabditis elegans* phenome mapping with an ORFeome-based RNAi library. *Genome Res* **14**, 2162–2168 (2004).

77. Han, S. K. et al. OASIS 2: online application for survival analysis 2 with features for the analysis of maximal lifespan and healthspan in aging research. *Oncotarget* **7**, 56147–56152 (2016).

78. Hulsen, T. DeepVenn: a web application for the creation of area-proportional Venn diagrams using the deep learning framework Tensorflow.js. *arXiv* preprint arXiv:2210.04597 (2022).

79. Bailey, T. L., Johnson, J., Grant, C. E. & Noble, W. S. The MEME Suite. *Nucleic Acids Res.* **43**, W39–W49 (2015).

80. Bailey, T. L. & Grant, C. E. SEA: simple enrichment analysis of motifs. Preprint at https://www.biorxiv.org/content/10.1101/2021.08.23.457422v1 (2021).

81. Witting, M., Maier, T. V., Garvis, S. & Schmitt-Kopplin, P. Optimizing a ultrahigh pressure liquid chromatography-time of flight-mass spectrometry approach using a novel sub-2μm core-shell particle for in depth lipidomic profiling of *Caenorhabditis elegans*. *J. Chromatogr. A* **1359**, 91–99 (2014).

82. Almanzar, D. E., Hamrick, A. & Rog, O. Single-sister labeling in the *C. elegans* germline using the nucleotide analog EdU. *STAR Protoc.* **3**, 101344 (2022).

Acknowledgements

Author contributions

A.C. and S.S.L. conceptualized the study and designed the experiment. A.C. performed the experiments. A.C. and S.S.L. interpreted the data and wrote the manuscript. S.S.L. supervised the study and acquired the funding.

Competing interests

The authors declare no competing interests.

Ethical approval

This study did not involve human participants, human tissue, or animals subject to ethical approval. Therefore, inclusion criteria related to sex, gender, or demographics are not applicable.

Additional information

Supplementary information The online version contains supplementary material available at https://doi.org/10.1038/s41467-025-64341-x.

Correspondence and requests for materials should be addressed to Siu Sylvia Lee.

Peer review information *Nature Communications* thanks the anonymous reviewers for their contribution to the peer review of this work. A peer review file is available.

Reprints and permissions information is available at http://www.nature.com/reprints

Publisher's note Springer Nature remains neutral with regard to jurisdictional claims in published maps and institutional affiliations.